BNL-227493-2025-JAAM

GRP-COSC-12

Ketjenblack-Supported and Unsupported ZrO2-ZrN Nanoparticle Systems for Enabling Efficient Electrochemical Nitrogen Reduction to Ammonia

M. Sharma, K. Sasaki

To be published in "ACS Applied Materials & Interfaces"

December 2024

Chemistry Department

Brookhaven National Laboratory

U.S. Department of Energy

USDOE Office of Energy Efficiency and Renewable Energy (EERE), Office of Sustainable Transportation. Hydrogen Fuel Cell Technologies Office (HFTO)

DISCLAIMER

Ketjenblack-Supported and Unsupported ZrO_2-ZrN Nanoparticle Systems for Enabling Efficient Electrochemical Nitrogen Reduction to Ammonia

Mitu Sharma,[1] Kotaro Sasaki,[2] Gary Halada,[3] Krishnakumari Pamula,[3]

Taejin Kim,[3] and Stanislaus S. Wong[1,*]

[1]Department of Chemistry, Stony Brook University, Stony Brook, New York 11794-3400, USA

[2]Chemistry Division, Brookhaven National Laboratory, Upton, New York 11973, USA

[3]Materials Science and Chemical Engineering Department, Stony Brook University,

Stony Brook, NY 11794-2275, USA

*To whom correspondence should be addressed.

E-mail: stanislaus.wong@stonybrook.edu

Keywords: zirconium oxide, zirconium nitride, nitrogen reduction reaction, ammonia, electrocatalysis, Faradic efficiency

Abstract – Artificial N_2 fixation via the electrocatalytic nitrogen (N_2) reduction reaction (NRR) has been recently promoted as a rational route towards reducing energy consumption and CO_2 emission as compared with the traditional Haber-Bosch process. Nevertheless, optimizing NRR relies on developing highly efficient electrocatalysts. Herein, we report on the reliable and reproducible synthesis of two promising electrocatalysts in either the presence or absence of Ketjenblack (KB), respectively, namely ZrO_2-ZrN@KB and ZrO_2-ZrN systems, synthesized through the nitriding of Zr. Both materials had never previously been considered for NRR, to the best of our knowledge. Nevertheless, both of these electrocatalysts incorporated a combination of tetragonal ZrO_2, ZrON, and cubic ZrN and showed excellent activity and durability towards NH_3 formation. Moreover, the maximum NH_3 production rate of 84.1 μg h^{-1} mg^{-1} at −0.7 V vs. a reversible hydrogen electrode (RHE) was achieved with the ZrO_2-ZrN electrocatalyst with an impressive Faradic efficiency of 21.2 % at −0.6 V vs RHE, indicating a high selectivity associated with the NRR. Additionally, the catalysts demonstrated excellent stability during the electrolysis process and recycling tests. We postulate that the combination of exposed active sites of ZrN and ZrO_2 likely contributes to the enhanced NRR performance attributed to ZrO_2-ZrN.

1. Introduction

Ammonia represents one of the largest carriers for the ubiquitous movement of renewable energy in addition to its other uses in the fertilizer and chemical industries.[1, 2] Currently, it is perceived as a potential replacement for carbon-based fuels, due to its high energy density (4.32 kW h L^{-1}), facile storage at low pressure, and easy transport.[1-6] The traditional thermochemical Haber-Bosch process has yielded immense advantages throughout the world.[7] However, the reliance of this process on high temperatures (400°C) and pressures (150−200 bar), which utilize about 2% of the global energy consumption, have propelled attempts to explore more sustainable alternatives for the generation of ammonia.[8] The electrocatalytic nitrogen reduction reaction (NRR) denotes one of the most promising alternative approaches to ammonia generation since it can be powered by electricity generated from renewable sources and can overcome the characteristic disadvantages of the energy-intensive Haber-Bosch process.[9, 10]

The similar potential region between the NRR and the reduction of water to form hydrogen results in the hydrogen evolution reaction (HER), which is the major competing reaction to NRR and leads to relatively low faradaic efficiencies of less than 1% toward NH_3.[9, 11] Due to the high ionization energy (15.6 eV) of the inert N≡N triple bond, and the slow reaction kinetics involving six proton-coupled electron transfer steps, an electrocatalyst is necessary to enable N_2 adsorption and activation in the NRR process.[4, 12] An operationally feasible catalyst for electrochemical ammonia synthesis should not only provide for sufficiently strong binding to facilitate N-N bond breaking but also prevent H-H bond association and allow for the protonation and removal of NH_3.[10, 11]

The transition metals are generally regarded as promising catalysts to alleviate the kinetic issues for N_2 activation, as they possess *d*-orbital electrons for π-electron back donation.[13, 14]

However, transition metal catalysts evince poor binding towards nitrogen and are not effective enough, in and of themselves for the N_2 activation process.[14, 15] Moreover, the *d* orbital electrons within transition metals also contribute to the formation of metal-H bonds for the hydrogen evolution reaction (HER).[14, 16-19] Therefore, improvements in electrocatalytic NRR are required not only in terms of developing and enabling a completely new class of catalysts but also for modifying existing catalysts to achieve novel mechanisms for effective N_2 activation.[14, 19-21]

Based on some recent studies, it has been suggested that the introduction of dopants and/or defects into transition metal nitrides (TMNs) can improve their electrocatalytic NRR performance by comparison with their undoped counterparts.[22, 23] For example, the introduction of an O atom onto the metal-N surface could be advantageous for the activation of the surface N sites adjacent to the surface O atom.[23] Specifically, the presence of surface O atoms can result in the regulation of the electronic structure of the nitride and a concomitant weakening of the metal–N bond. These plausible scenarios could thereby lead to the lowering of the energy barrier for NH_3 release and consequently facilitate the progress and optimization of NRR. On the other hand, in stable compounds of Zr such as ZrO_2, the central element of zirconium possesses a vacant orbital suitable to accept lone pair electrons of the N_2 molecule σ orbital, which significantly weakens the N≡N bond.[24, 25] Therefore, the strategic modification of the TMN electron state either using the relevant oxide alone or introducing a metal oxide impurity could plausibly assist in accomplishing and enabling high NRR performance.[23, 26]

Via comprehensive density functional theory-based analysis, several theoretical studies have been proposed to study a relatively unexplored family of promising and cost-efficient catalysts, namely TMNs for NRR.[27-31] However, to the best of our knowledge, associated experimental measurements along with the practical, real-life application of most TMNs in the

context of the electrochemical reduction of N_2 to NH_3 are still scarce. For instance, Xiao et al. demonstrated that ZrN_6 can effectively promote the nitrogen fixation process under the limiting potentials of 0.51 V, using DFT calculations.[31] In a separate study, Pilania and coworkers performed DFT computations to investigate the effect of surface compositional and configurational changes, namely the presence of surface oxygen and surface steps, upon the catalytic activity of ZrN for the electrochemical NRR process occurring through the Mars–Van Krevelen (MvK) mechanism.[30]

Within the MvK mechanism, the lattice N atoms are reduced to NH_3 and are desorbed from the surface; consequently, a surface N vacancy species is generated, which is subsequently replenished by absorbing an N_2 molecule. According to their computational results, the pristine and the oxynitride surfaces of ZrN revealed a qualitatively similar potential energy surface profile for the elementary reaction mechanism.[30] Talarmin et al. and Skúlason et al. noted that either VN, NbN, CrN, or ZrN can reduce nitrogen to ammonia via the MvK mechanism at smaller overpotentials of around −0.5 to −0.8 V by comparison with pure transition metals, wherein higher overpotentials of around −1.0 to −1.5 V were predicted to form ammonia.[27-29, 32]

In a comprehensive DFT-based computational screening of TM mono-nitrides with 26 different *d*-block metal ions, Abghoui et al. found that the most promising candidates comprise the (100) facets of the rock-salt (RS) structure of VN and ZrN, which show a likelihood for generating ammonia in high yields at lower onset potentials and in principle, exhibit zero poisoning by oxygen, hydroxide, and hydrogen species.[27, 30, 33] In their complementary, computational work, Pilania and co-workers evaluated and compared the energetics of the ZrN (100) step and zirconium oxynitride (100) flat surfaces for the NRR elementary reactions and found that the oxynitride surface gave rise to a favorable 30 meV lower overpotential as

compared with that of the pristine ZrN surface.[30] On the other hand, the ZrN step surface exhibited a 40 meV higher overpotential, due to a stronger binding of N_2 on the surface vacancy.[30] Moreover, Skúlason highlighted the RS(111) nitrides as being the most favorable in terms of H adsorption on a surface N with the least affinity of H binding to neighboring metal atom(s), a process that would thereby facilitate NRR on the surface.[27] It has been hypothesized by Yang et al. that the metal oxynitride acts as an active phase for electrochemical NRR, because of the presence of active surface N sites adjacent to the surface O atoms.[26] Furthermore, Guo and Li et al. demonstrated the ability of the ZrO_2/C electrocatalyst to reduce nitrogen to ammonia via the formation of Zr-N species during NRR.[25] Collectively, materials incorporating all the different phases of ZrN, ZrON, and ZrO_2 can be credibly assumed to act as dynamic electrocatalysts toward NRR.

It is worth noting that many of these previous reports have demonstrated the practical electrocatalytic applicability of VN.[26, 34-36] However, analogous studies of the experimental applicability of either ZrN, ZrON, ZrO_2, or a merged ZrO_2-ZrN system toward NRR are still somewhat limited. Therefore, we selected a combination electrocatalyst comprised of mainly ZrN and ZrO_2, based on the prior body of DFT studies and previous literature findings which have provided a legitimate rationale with which to value the promise and potential of this material as an electrocatalyst towards NRR for producing ammonia. [27, 29]

Moreover, the ZrO_2-ZrN catalyst maintains a stable N-vacancy at the surface and should not be poisoned by either oxygen or hydrogen from the aqueous electrolyte.[29] At the onset potential, the N-vacancy is stable towards both protonation and oxidation from water, and it can easily react with atmospheric nitrogen injected into the system under ambient conditions.[27, 29] Thus, the competing HER could be suppressed to a large extent, and a significant amount of

ammonia production should be expected.[28, 29] Hence, based on the above-mentioned findings and precedence, herein we report on the synthesis of a promising zirconium-based (ZrO_2-ZrN) platform in addition to an analogous system composed of zirconium ZrO_2-ZrN deposited onto conductive carbon (ZrO_2-ZrN@KB) for the efficient reduction of N_2 to NH_3.

2. Experimental section

2.1. Materials

Zirconium tetrachloride (Sigma Aldrich), Mg powder (Alfa Aesar), Ketjenblack carbon (AKZO Nobel LLC; EC600-JD), Nafion solution (5 wt. % in water and ethanol mixture) (Beantown Chemical), Toray carbon paper- 30% wet proofing (Fuel Cell Earth), salicylic acid (Thermo Scientific), ammonium chloride (Thermo Scientific), sodium citrate dehydrate (Fisher Chemical), sodium hypochlorite solution (NaClO, 5%) (Fisher Chemical), sodium nitroferricyanide dihydrate ($C_5FeN_6Na_2O \cdot 2H_2O$) (LabChem), sodium hydroxide (NaOH) (Acros Organics), and hydrochloric acid (HCl) (36.5-38 %, Alfa Aesar) were used, as received. In particular, all reagents were of analytical reagent grade and utilized without further purification. Ultrapure water (18.2 MΩ cm^{-1}) was produced by a Milli-Q ultrapure system throughout all of the experiments.

2.2. Synthesis of tested electrocatalysts

2.2.1 Synthesis of ZrO_2-ZrN@KB and ZrO_2-ZrN catalysts

The conductive carbon-containing ZrO_2-ZrN@KB electrocatalyst was prepared by mixing in 0.32 g of $ZrCl_4$, 0.34 g of Mg powder, and 0.3 g of Ketjenblack (KB) in 30 mL ethanol by a process of ultrasonication and stirring. In this synthesis, the Mg powder was used as a reducing agent.[37] The mixture was then dried using a rotary evaporator. The as-obtained powder was then transferred to an alumina crucible and subjected to annealing by passing Ar for 30 min

followed by NH_3 for 6 h at 850°C at a flow rate of 1 L/min to induce nitridation within a quartz tube furnace.[37] After 8 h, the sample was cooled inside the tube furnace, and Ar gas was allowed to flow in overnight to eliminate any toxic gases. The nitridation product was then washed with 1.5 M HNO_3 and ethanol to remove any unwanted byproducts and subsequently dried in a vacuum furnace at 50°C for 12 h to obtain the desired ZrO_2-ZrN@KB powder. The pristine ZrO_2-ZrN electrocatalyst was prepared by employing an identical synthesis method to that of ZrO_2-ZrN@KB but in the absence of KB.

2.3. Preparation of the Working Electrode. 10 mg of either ZrO_2-ZrN@KB or ZrO_2-ZrN was dispersed in a mixed solution, consisting of 700 μL H_2O, 200 μL isopropyl alcohol, and 100 μL Nafion (5 w%), which was then sonicated for 1 h to form a homogeneous ink. Subsequently, 10 μL of the ink was loaded onto a carbon paper with an area of 1 cm × 1 cm (catalyst mass loading of 0.1 mg cm^{-2}) and dried under ambient conditions. Thus, the working electrodes obtained for these inks were named C- ZrO_2-ZrN@KB and C- ZrO_2-ZrN, respectively, whose specific preparation followed that of accepted protocols in the prior literature.[23, 38, 39] As the catalyst loading was only 0.1 mg cm^{-2} and an adequate amount of Nafion was used, the catalyst stuck to the carbon cloth throughout the experiments and no falling of ZrO_2-ZrN@KB or ZrO_2-ZrN during NRR was observed from the working electrode.

2.4. Characterization

2.4.1. Scanning electron microscopy: SEM images were collected with the JEOL JSM-7600F scanning electron microscope, equipped with an energy dispersive spectrometer (EDS) at an accelerating voltage between 5 and 10 kV. The ZrO_2-ZrN@KB and ZrO_2-ZrN samples were prepared for SEM imaging by dispersing in 5 mL of ethanol by sonication and then drop-casting in small aliquots onto silica wafers prior to drying at room temperature.

2.4.2. Transmission electron microscopy: TEM images were collected with the JEOL 1400 transmission electron microscope at accelerating voltages between 80 and 120 kV, equipped with a 2048 × 2048 Gatan charged-coupled device (CCD) camera. The HRTEM and STEM data were collected using an FEI Talos 200x, an operando Scanning Transmission Electron Microscope. The ZrO_2-ZrN@KB and ZrO_2-ZrN samples were prepared for TEM imaging by dispersing in 5 mL of ethanol via sonication and drop-casting aliquots onto copper grids which were coated with lacey carbon. The particle sizes were calculated using ImageJ software.

2.4.3. Raman spectroscopy: Raman spectral analysis for ZrO_2-ZrN@KB and ZrO_2-ZrN samples was performed under ambient conditions using a Horiba Raman Microscope (Xplora Plus, Horiba Instruments Inc., Piscataway, NJ, USA). The Raman spectra were collected using a laser source of 532 nm with an output power of 5 mW and a 10x (NA = 0.25) objective. The acquisition time of 30 seconds and accumulations of 10 scans were maintained throughout the measurements. Systematic scans were conducted on each sample at various positions to investigate the variations in the oxide crystal structure and composition across the oxide thickness. Data processing was carried out using the Jobin Yvon LabSpec 6 instrument.

2.4.4. X-ray Diffraction: XRD analysis was conducted on a Rigaku Mini Flex 600 X-ray diffractometer. The instrument was operated at voltage-current conditions of 40 kV and 15 mA, using Cu Kα radiation (λ = 1.5406Å). The sample was prepared by sonicating the ZrO_2-ZrN@KB and ZrO_2-ZrN powder, dispersed in 5 mL of ethanol. Small aliquots of the sample were then drop cast onto a Si zero background diffraction plate for XRD. Measurements were subsequently collected from 2θ values of 10°– 80°at a rate of 4°/min, and the XRD patterns were analyzed by using the Match! Program and the underlying JCPDS file no. 42-1164.

2.4.5. X-ray photoelectron spectroscopy (XPS): X-ray photoelectron spectroscopy (XPS) measurements were conducted on a Physical Electronics Quantum 2000 XPS microprobe instrument, capable of chemical mapping. It is equipped with a 16-channel detector, a flood gun for charge compensation (thereby facilitating analysis of surfaces with limited conductivity), and an ion gun for chemical profiling. Monochromatic Al K α X-rays (1486.6 eV) were used at 12.5 W, with a beam diameter of 50 microns. The neutralizer was set at 1.0 V and 20 microamps, and the analyzer was used in the Fixed Analyzer Transmission (FAT) mode. Calibration due to charging considered the adventitious C 1*s* peak binding energy to be at 284.6eV. Data deconvolution was conducted with PHI MultiPak software (version 9.1.1), utilizing a Shirley background for all peaks.

2.4.6. Nuclear Magnetic Resonance (NMR): The NMR data were acquired on a 500 MHz spectrometer upgraded with a Brüker Avance III Console with a variable temperature accessory, a digital temperature control unit, and Z-gradient electronics. The samples were run for 1024 scans with 4 control scans, performed at room temperature.

2.5. Electrochemical Measurements

The electrochemical experiments were performed on a potentiostat (SP-300, Bio-Logic Science Instruments Ltd.) using either C- ZrO_2-ZrN@KB or C- ZrO_2-ZrN, an Ag/AgCl electrode (3M KCl electrolyte), and a platinum sheet as the working, reference, and counter electrodes, respectively. An H-shaped electrolytic cell isolated by a Nafion 211 membrane in the middle was used to conduct the NRR tests, as shown in **Scheme S1**. The potential utilized was converted to a reversible hydrogen electrode (RHE) scale by calibration using the equation: E (vs RHE) = E (vs Ag/AgCl) + 0.207 V. The corresponding current density was normalized to the geometric surface area. For conducting the electrochemical N_2 reduction, the chronoamperometry tests (−0.8 to

−0.3 V vs. RHE for ZrO_2-ZrN@KB and -0.8 to -0.5 V vs. RHE for ZrO_2-ZrN were performed in an N_2 (99.9%)-saturated 0.1 M HCl solution, which was purged with N_2 for approximately 30 min before running the NRR experiment.

2.6 . Determination of Ammonia (NH_3).

The concentration of NH_3 generated after each NRR experiment run was spectrophotometrically measured by employing the indophenol blue method.[38-40] Specifically, 2 mL of electrolyte was taken from the cathodic chamber, and then a combination of 2 mL of chromogenic reagent (1 M NaOH, 5 wt.% $C_7H_6O_3$, 5 wt.% $C_6H_5Na_3O_7$), 1 mL of oxidizing solution (0.05 M NaClO), and 0.2 mL of catalyzing reagent (1 wt.% $Na_2[Fe(CN)_5NO]$) was sequentially added into this solution. The mixture was allowed to stand in the dark at room temperature for 2 h, and then the UV−vis absorption intensity was measured at 655 nm. The reaction scheme for the formation of indophenol is shown in **Figure S1**. The concentration vs absorbance curves were calibrated using the standard NH_4Cl solution (**Figure S2**) with a series of different concentrations. The fitting curve ($y = 0.077x + 0.0148$, $R^2 = 0.998$) yielded an excellent linear correlation between absorbance values and measured NH_4Cl concentrations.

2.7 Determination of Hydrazine (N_2H_4)

The Watt and Chrisp method was used to estimate the amount of N_2H_4 formed in the electrolyte.[41] A color reagent was prepared by mixing para-(dimethylamino)benzaldehyde (PDAB) (5.99 g) in 0.1 M HCl (30 mL) in ethanol (300 mL) along with a 5 mL of electrolyte to which was added 5 mL of the prepared color reagent. **Figure S3** highlights the reaction of hydrazine with PDAB to form a yellow-colored azine complex, which is stable under acidic conditions. This mixture was then stirred for 30 min at room temperature, and the absorbance was measured at 455 nm using a UV−vis spectrometer (**Figure S4 (a)**). A standard curve was

plotted using a series of standard hydrazine solutions incorporating different N_2H_4 concentrations of 0.05, 0.1, 0.15, 0.2, 0.3, 0.4, and 0.5 μg mL^{-1}, respectively, in 0.1 M HCl. The fitting curve (**Figure S4 (b**)) evinced an excellent linear relationship between absorbance versus N_2H_4 concentrations ($y = 0.2486 x + 0.0116$, $R^2 = 0.999$). This curve was used to calculate the yields of hydrazine in the electrolyte.

2.8 Calculation of V_{NH3} and Faradaic Efficiency (FE)

The rate of NH_3 formation (V_{NH3}) was calculated using **Equation 1.**[25, 38, 39]

$$V_{NH3} = \frac{V \times [NH_3]}{t \times m_{cat}} \quad (1)$$

The corresponding Faradaic efficiency (F.E.) was calculated using **Equation 2**.[25, 38, 39]

$$F.E. = \frac{3F \times V \times [NH_3]}{Q \times 17} \quad (2)$$

In these equations, V is the volume of the electrolyte; $[NH_3]$ is the concentration of NH_3; t is the electrolysis time; m_{cat} is the catalyst mass; 3 denotes the number of electrons transferred per ammonia molecule; F is the Faraday constant; Q is the theoretical electronic quantity across the electrode, and 17 represents the molar mass of ammonia (i.e., 17 g/mol).

3. Results and Discussion

The syntheses of ZrO_2-ZrN@KB and ZrO_2-ZrN were achieved by a nitridation process in which either the mixture of $ZrCl_4$, Mg powder, and KB (for ZrO_2-ZrN@KB) or a corresponding mixture of $ZrCl_4$ and Mg powder alone (for ZrO_2-ZrN) was combined in ethanol under stirring and centrifugation prior to drying in order to generate a homogeneous black powder. The KB was used to provide for a larger specific surface area (1400 m^2 g^{-1}) and a superior conductivity to

the electrocatalyst ZrO_2-ZrN@KB.[42-45] The powder was then subjected to the nitridation process by passing NH_3 to form either ZrO_2-ZrN@KB or ZrO_2-ZrN, wherein the dispersed N atoms adjacent to the O atoms provided extra reactive sites to the overall electrocatalyst.[26] The extraneous Mg content and other potential impurities were eliminated by washing the final ZrO_2-ZrN@KB and ZrO_2-ZrN with HNO_3 and ethanol. The schematic representation for the synthesis of ZrO_2-ZrN@KB is shown in **Figure 1**.

3.1. Microscopy and Spectroscopy Characterization of ZrO_2-ZrN@KB and ZrO_2-ZrN

To analyze the morphology of ZrO_2-ZrN@KB and ZrO_2-ZrN, we utilized scanning electron microscopy (SEM) and transmission electron microscopy (TEM). The SEM image of ZrO_2-ZrN@KB (**Figure 2a**) showed that ZrO_2-ZrN@KB possessed layered structures, likely composed of many large plates of KB with Zr, O, and N dispersed all over the surface of KB, as can be deduced from the EDS mapping data presented in **Figure 2 b, c, d, f**. It has also been observed that some ZrO_2-ZrN particles are also slightly aggregated on certain areas on the external surface of KB. The SEM and EDS mapping images of ZrO_2-ZrN (**Figure 3 a, b c, d, e**) showed that the Zr, O, and N are distributed within the as-prepared sample. However, EDS analysis on compositions of Zr, O, and N was difficult for both ZrO_2-ZrN@KB and ZrO_2-ZrN, likely due to the apparently uneven distribution of ZrO_2 and ZrN species throughout the surface of the tested samples.

The corresponding TEM images of ZrO_2-ZrN@KB catalysts are provided in **Figure 4 (a).** The isolated ZrO_2-ZrN particles (dark color spheres) appear to be well dispersed within a KB carbon background (gray color).[46-48] The average size of the isolated ZrO_2-ZrN particles was ~5.4 ± 1.4 nm, as shown in the histogram in **Figure S5 (A**). For further confirmation of the particle size and crystallinity, we collected complementary STEM and HRTEM data, as shown in

Figure 4 (b) and **(c)**. The observed lattice spacings, as seen in the HRTEM, are ~0.29 nm in dimension, which can be ascribed to the (110) plane of the tetragonal structure of ZrO_2 present in ZrO_2-ZrN@KB.[25] It is worth highlighting that no distinctive ZrN or ZrON species were identified in the HRTEM images of ZrO_2-ZrN@KB. As a result, no lattice fringe of ZrN or ZrON was observed. This could be ascribed to the poor nitridation within ZrO_2-ZrN@KB due to the interference of KB with NH_3 during the nitridation process. The corresponding TEM images of ZrO_2-ZrN are shown in **Figure 5 (a)**. The average size of the particles was found to be ~11.8 ± 2.3 nm, as shown in the histogram presented in **Figure S5(B)**. For further confirmation of the particle size and crystallinity, we collected complementary STEM and HRTEM data, as shown in **Figure 5 (b)** and **(c)**. The structural postulate of a ZrN core coupled with an oxidized ZrO_2 shell was revealed by the presence of lattice spacings of 0.22 nm and 0.29 nm, corresponding to the (200) planes of cubic ZrN within the core and the (110) planes of the tetragonal ZrO_2 localized in the outer shell.[49-51] However, the clear identification of ZrON species within the sample was not obvious in the HRTEM image data associated with ZrO_2-ZrN.

With respect to chemical composition, the as-obtained XRD peak values of ZrO_2-ZrN@KB nano-particles of 30.62º, 35.56º, 51.07º, 60.63º, and 74.43º correspond to Miller indices of (101), (110), (112), (211), and (220), respectively, associated with the JCPDS file no. 89–7710 and consistent with the tetragonal phase of ZrO_2 (**Figure S6 (a)**).[48, 52-57] The characteristic diffraction peaks of KB were observed at 21.58° and 45.80°, which can be indexed to the (002) and (100) crystallographic carbon planes, respectively (**Figure S6 (a)**).[58, 59] A small portion of the ZrO_2-ZrN@KB contains ZrN, a finding which was implied by the presence of small peaks at 34.45º and 39.95° (**Figure S6,** blue dotted line) ascribed to Miller indices of (111) and (200), respectively.[54, 57, 60]

For the ZrO_2-ZrN catalyst alone, the peaks centered at 2θ values of 34.45°, 39.95°, 57.60°, 68.76°, and 72.36° could be attributed to the (111), (200), (220), (311), and (222) crystalline planes of the cubic phase of ZrN, respectively (**Figure S6 (b)**).[54, 57, 60] Herein, small peaks associated with ZrO_2 were observed at 30.62°, 51.07°, and 60.63°, and likely are associated with Miller indices of (101), (112), and (211) (**Figure S6,** yellow dotted line), respectively.[48, 52-57] From the XRD analysis, no apparent peak for ZrON was observed within both of the ZrO_2-ZrN@KB and ZrO_2-ZrN catalyst samples.

The Raman spectral data collected at specific locations for ZrO_2-ZrN@KB and ZrO_2-ZrN are presented in **Figures S7 (a) and S7 (b)**. The Raman spectra of ZrO_2-ZrN@KB demonstrated the presence of several peaks consistent with the occurrence of the tetragonal phases of ZrO_2, ZrN, and KB, respectively (**Figure S7 (a)**). The peaks located at 143, 170, 252, 315, 445 cm^{-1}, and 627 cm^{-1} are connected to the tetragonal phase of ZrO_2.[61-64] A very small peak situated at ~567 cm^{-1} could be assigned to the weak asymmetric band of ZrN. Moreover, the increased intensity of the peak at 143 cm^{-1} and the splitting of the peak at ~252 cm^{-1} could be collectively attributed to the presence of vibrational modes of ZrN.[65, 66] For KB, two distinctive Raman bands corresponding to the D and G bands were noted at 1340 and 1597 cm^{-1}, respectively. The D band nominally designates the out-of-plane vibrations, due to either disorder or defects in the lattice, whereas the G band is the so-called graphene band that details the in-plane stretching vibrational profile of the C–C bond (first-order E_{2g} symmetry mode).[58, 67] Moreover, since a small number of N atoms are supposedly dispersed over the entire surface of ZrO_2 on KB (as per SEM-EDS), it is not surprising that the signals ascribed to KB and t-ZrO_2 appear to be more dominant than those associated with ZrN itself. The Raman spectrum of ZrO_2-ZrN, as shown in **Figure S7 (b)**, highlighted characteristic peaks at 180, 223, 508, and 660 cm^{-1}, corresponding to ZrN, implying

that the core ZrN species is present within ZrO_2-ZrN, a finding which correlates well with the previously discussed XRD and TEM results.

The complementary X-ray photoelectron spectroscopy (XPS) analysis of **ZrO_2-ZrN@KB** (**Figure S8 (a)**) indicated perceptibly little N *1s* signal in the survey spectrum, which is not unexpected, due to the relatively low detection limit of N. The overall spectra, however, suggested the occurrence of both O *1s* and Zr *3d* peaks which are consistent with the presence of the tetragonal phases of the ZrO_2 structure (**Figure S8 (a)**). The Zr *3d* regions are revealed in **Figure S8 (b)**, which highlights doublets associated with ZrN (179.7 eV (Zr $3d_{5/2}$) /182.2 eV (Zr $3d_{3/2}$)), ZrON (180.8 eV (Zr $3d_{5/2}$) /183.3 eV (Zr $3d_{3/2}$)), and ZrO_2 (182.2 eV (Zr $3d_{5/2}$) /184.6 eV (Zr $3d_{3/2}$)). The positions for Zr *3d* binding energies are consistent with that previously reported by Rizzo *et al*. for ZrO_2 and ZrN_xO_y, although they reported a slightly higher binding energy for ZrN (i.e., 180.2 eV for the Zr $3d_{5/2}$ singlet).[54] While the relative size of the nitride peak as compared with the other Zr species appears to be significant, the survey spectrum from this sample indicates only a relatively small Zr *3d* contribution overall (as compared with the very large C *1s* contribution from the KB, which dominates the spectrum).

It is also worth noting that the N *1s* spectra (as shown in (**Figure S8(a)**) is almost impossible to resolve, due to a very low signal-to-noise ratio. The O *1s* spectra from the ZrO_2-ZrN@KB sample demonstrate the presence of two peaks, as shown in **Figure S8 (c)**, corresponding to ZrO_2 (530.0 eV) and ZrON (531.1 eV). A third larger peak located at about 532.7 eV can be correlated with O bound to C (as noted in the C*1s* spectrum), but may also include a contribution from water adsorbed onto the surface from adventitious sources.[25, 68-71] The N 1*s* spectra for ZrO_2-ZrN@KB are shown in **Figure S8 (d)**, wherein the three peaks fitted are consistent with an N *1s* fit with a peak located at 395.4 eV corresponding to ZrN; a signal

positioned at 397.8 eV associated with ZrON, in addition to a third peak situated at ~400 eV, which might represent a more oxidized N species from the interfacial region between the nitride and the oxynitride. Moreover, the C *1s* peak appearing at 286.5 and 285.4 eV implies some degree of contributions from the oxidized C=O and C-O bonds, respectively (**Figure S8 (e)**).[25, 68, 69] A peak attributed to a C-C bond is also observed at 284.5 eV.[72]

The survey spectrum from the ZrO_2-ZrN powder (**Figure S9(a)**), which does not incorporate KB, on the other hand, shows a relatively large Zr *3d* peak (as compared to any C resulting from adventitious sources) along with correspondingly well-resolved O *1s* and N *1s* peaks. Hence, as shown in **Figure S9(b)**, the Zr *3d* peak can be resolved into components of ZrN, ZrON, and ZrO_2.[73, 74] The expected peaks for (i) the ZrN bonds at 179.8 eV (Zr $3d_{5/2}$) and at 182.4 eV (Zr $3d_{3/2}$); (ii) the ZrON bonds at 181.5 eV (Zr $3d_{5/2}$) and 184.0 eV (Zr $3d_{3/2}$); as well as (iii) the ZrO_2 bonds at 182.1 eV (Zr $3d_{5/2}$) and 184.6 eV (Zr $3d_{3/2}$) were observed.[73, 74] Interestingly, the Zr *3d* doublet related to ZrON (which may represent an interfacial species between a ZrN core and Zr oxide shell) is shifted to a slightly higher binding energy by about 0.5 eV. The reason for this finding is not obvious (although it may represent a shift of electron energy density away from Zr, perhaps due to N deficiency within this interfacial region); however, it is consistent with the O *1s* fit, as shown in **Figure S9 (c)**, which indicates a significantly larger ZrON: ZrO_2 ratio as compared with the spectra obtained from the ZrO_2-ZrN@KB sample. The peaks present in the O *1s* spectra from the ZrO_2-ZrN sample are consistent with those reported and identified by Cubillos *et al.* for ZrO_2 (529.5 eV), ZrO_xN_y (531.1 eV), and adsorbed water at the surface (532.7 eV).[75] Likewise, the N *1s* spectrum shown in (**Figure S9 (d)**, which can be more easily resolved due to the relatively larger signal as mentioned earlier, displays the presence of both ZrN (395.1 eV) and ZrON (398.0 eV) species.

The N *1s* value for ZrN is consistent with that reported for N that is four-coordinated to Zr (ZrN_2),[76] although it can vary significantly, based on variability in the degree of the N coordination within thin layers. Similarly, the values for the N *1s* photoelectron singlet for zirconium oxynitride can range from 397.5 to 400 eV, with small variations in the O: N ratio.

Overall, based on the characterization results, it can be concluded that although both of the catalysts tested consist of a mixture of ZrO_2, ZrN, and ZrON, ZrO_2 signifies the dominant surface species within ZrO_2-ZrN@KB, whereas both ZrO_2 and ZrN appear to be well mixed within the ZrO_2-ZrN material analyzed. More specifically, a core-shell motif is proposed for the ZrO_2-ZrN nanomaterial structure, based in particular on the HR-TEM data. The poor extent of nitridation within ZrO_2-ZrN@KB could be attributed in principle to the presence of the interference of KB with NH_3 during the nitridation process, whereas in the absence of KB within ZrO_2-ZrN, the nitridation process was comparatively more successful.

3.2. Electrocatalytic NRR Performance of ZrO_2-ZrN@KB and ZrO_2-ZrN

The as-synthesized ZrO_2-ZrN@KB and ZrO_2-ZrN catalysts were painted onto carbon paper (CP) with a mass loading of 0.1 mg cm^{-2} to construct the cathode electrodes (i.e., C- ZrO_2-ZrN@KB and C- ZrO_2-ZrN) for NRR within the H-shaped electrolytic cell. The linear sweep voltammetry curves for C- ZrO_2-ZrN@KB and C- ZrO_2-ZrN within Ar- and N_2-saturated 0.1 M HCl solution are illustrated in **Figure S10 (a)** and **Figure S10 (b),** respectively. It was found that the current density in the N_2-saturated solution was higher than that noted with the Ar-saturated solution in both cases. Our data demonstrate that the electroreduction of N_2 to NH_3 occurred with an onset potential of around −0.6 V on the C- ZrO_2-ZrN@KB and -0.7 V on the C- ZrO_2-ZrN electrode surface.

Comparable results have been detected for other analogous metal nitrides. For example, the performance of a CBN/CP catalyst indicated that the electroreduction of N_2 to NH_3 occurred with an onset potential of ~ −0.5 V.[38] For a VN nanosheet array on Ti mesh, the corresponding overpotential was also recorded at ~ -0.6 V. [34] Zheng and Sun *et al.* found that for the MoN nanosheet array, the measured onset potential was only ~ -0.3 V.[77] Moreover, based upon the computational studies by Abghoui and Skúlason, it was suggested that the N_2 reduction to NH_3 process occurs at a smaller bias of −0.5 V to −0.8 V in which the reaction can be explained by the MvK mechanism for VN, NbN, ZrN, and CrN electro-catalysts.[28]

The electrochemical data for the reduction of N_2 to NH_3 using ZrO_2-ZrN@KB and ZrO_2-ZrN as electrocatalysts are highlighted in **Figure 6** and **Figure 7**. The chronoamperometry curves (i.e., time-dependent current density curves) of C- ZrO_2-ZrN@KB and C- ZrO_2-ZrN evinced a level of reasonable stability at various potentials, as illustrated in **Figure 6(a)** and **Figure 7 (a)**. The current density started at a high current for all of the different potentials (-0.3 V to -0.8 V for ZrO_2-ZrN@KB and -0.5V to -0.8 V for ZrO_2-ZrN) but quickly dropped down and leveled off, before attaining a threshold value. This observation might be attributed to the charging of the double layer and a local concentration reduction of H^+ and N_2 near the electrode surface.[38, 39, 78, 79]

The electrolysis process was run for 3 h, and after 3 h, the as-generated NH_3 dissolved in 0.1 M HCl electrolyte was detected by the indophenol blue method.[36, 40] In the indophenol method, the concentration of the as-generated NH_3 was analyzed and quantified by analyzing the absorbance profile at 655 nm. **Figure 6 (b)** and **Figure 7 (b)** display the UV−visible spectra of the resulting electrolyte after the chromogenic reaction. Based on the corresponding calibration curves ($y = 0.077x + 0.0148$, $R^2 = 0.998$, **Figure S2**), the mass of as-generated NH_3 per hour and

per microgram of the catalyst, in addition to the V_{NH3} and FE results, were calculated, and the associated results are provided in **Figure 6 (c), Figure 7 (c), Table 1,** and **Table 2**.

It can be observed that with ZrO_2-ZrN@KB, the measured V_{NH3} is highest (61.2 μg h^{-1} mg^{-1}) at an applied potential of -0.6 V and is characterized by a lower value of 24.3 μg h^{-1} mg^{-1} at -0.8 V. Similarly, for ZrO_2-ZrN, the highest measured V_{NH3} reached a highly attractive figure of 84.1 μg h^{-1} mg^{-1} at -0.7 V, while at -0.8 V, the as-obtained V_{NH3} was only 52.1 μg h^{-1} mg^{-1}. The detected drop in the degree of NH_3 formation from -0.6 to -0.8 V in ZrO_2-ZrN@KB and -0.5 to -0.8 V in ZrO_2-ZrN could be attributed to the competing presence of the hydrogen evolution reaction at more negative potentials. Moreover, for ZrO_2-ZrN, above the potential of -0.5 V, no reduction was observed. At -0.9 V, only HER was observed, resulting in an unstable chronoamperometry curve. For ZrO_2-ZrN@KB, the highest FE of 1.54% was detected at a value of -0.4 V, while the lowest FE of 0.05 % was observed at -0.8 V. By contrast, for ZrO_2-ZrN, the highest FE measured reached 21.2% at -0.6 V, and the lowest FE detected was 2.05 % at -0.8 V (**Table 1** and **Table 2**). The lower FE measured at a value of -0.8 V could be ascribed to the increased theoretical electronic quantity expected ($FE \propto 1/Q$) across the electrode, which was measured at a higher potential.

As shown in **Table S1,** a number of prior studies on NRR using metal nitrides have been conducted, by means of comparison. Most of these metal nitride-catalyzed NRR processes utilized transition metals but reports on Zr-based metal nitrides are still rare. As is apparent from **Table 1** and **Table 2,** the performance of ZrO_2-ZrN@KB and ZrO_2-ZrN in selectively yielding NH_3 alone is either superior to or comparable to the activities of other metal nitride-based catalyst systems, reported thus far. It is to be noted that the NH_3 yield rate of ZrO_2-ZrN outperforms that of ZrO_2-ZrN@KB possibly due to the higher activity of ZrO_2-ZrN in

comparison to ZrO_2-ZrN@KB which can be potentially attributed to the relatively greater number of ZrN sites present in ZrO_2-ZrN as compared with ZrO_2-ZrN@KB. The relatively greater content of ZrN formed within ZrO_2-ZrN could have resulted from the more easily accessible and reactive surface of Zr during the nitriding procedure as compared with the ZrO_2-ZrN@KB composite, which was covered with KB on its surface.

Moreover, the presence of KB could hinder the availability and spatial accessibility of the active ZrN sites which are fewer in number within ZrO_2-ZrN@KB. Thus, further increasing the content of KB in ZrO_2-ZrN@KB could significantly decrease the NRR activity. According to previous findings and computational studies performed on the NRR mechanism on metal nitrides, the behavior of ZrO_2-ZrN is proposed to follow the MvK mechanism in which the N atoms of ZrN are reduced to NH_3 and are desorbed from the surface; subsequently, the as-generated surface N vacancy can next be replenished by absorbing an N_2 molecule, and hence, in principle, the cycle can continue to generate additional NH_3 molecules.[28, 30]

In an attempt to confirm that obtained NH_3 is *only* derived from NRR associated with C-ZrO_2-ZrN@KB and C- ZrO_2-ZrN species alone and not from competing processes, we also conducted two control experiments. First, we immersed the sample within an N_2-saturated solution without applying any voltage for 3 h, and in the second experiment, we immersed the sample within an Ar-saturated solution at a value of –0.3 V for 3 h. Apparently, no production of NH_3 was evident in either experiment for these two electrocatalysts.

In order to check the effect of an alkaline medium, we also conducted the NRR experiment in 0.1 M KOH keeping all the other parameters intact for the ZrO_2-ZrN catalyst. At a potential of -0.7 V for 3h, the ZrO_2-ZrN catalyst did not show sufficient NRR activity. This could be due to the competing OH^- ions with N_2 molecules for active sites on the catalyst leading to

less adsorption of N_2 molecules on the catalyst surface.[80, 81] This could lead to lower activity of the catalyst toward the production of NH_3 in an alkaline medium.

Moreover, we checked the electrocatalytic activity of the catalyst ZrO_2-ZrN in nitrate reduction reaction (NORR) following a similar method to the NRR. The electrolysis process was run for 3 h, at -0.7 V in a mixture of 0.1 M KNO_3 and 0.1 M HCl, and after 3 h, the as-generated NH_3 was detected by the indophenol blue method. It was noted that the chronoamperometric curve showed reasonable stability, however, for the indophenol test the UV-vis spectra do not show any peak around 655 nm indicating no production of NH_3. The corresponding chronoamperometric curve and the UV-vis spectra are shown in **Figure S11.**

Since the NRR activity of ZrO_2-ZrN was noted to be higher than that of ZrO_2-ZrN@KB, we chose to conduct a time-dependent study on the NRR using the C- ZrO_2-ZrN catalyst at -0.7 V, keeping all the other reaction parameters intact (**Figure S12** and **Table S2**). Specifically, we ran the NRR at different time intervals, spanning from 0.5 to 5 h. It was observed that the formation of NH_3 increased from a concentration of 0.35 μg/mL at 0.5 h to 0.63 μg/mL at 3h and that this value gradually decreased to 0.47 μg/mL at 5 h (**Figure S12**). The slight reduction in the concentration of NH_3 that was measured with increasing reaction time could be potentially attributed to the slight decay of the cathodic current.[82] However, the measured rate of NH_3 formation, i.e. V_{NH3}, of 282.4 $\mu g_{NH3}\, h^{-1}\, mg^{-1}$, was found to be the highest at an interval of 0.5 h of reaction time associated with a high FE of 18.7% (**Table S2**).

The stability of an electrocatalyst and its corresponding potential for regeneration and reusability is certainly of major importance for deducing its practical utility. Hence, the stability and durability of the electrocatalysts, i.e., ZrO_2-ZrN@KB and ZrO_2-ZrN, were also evaluated by measuring the chronoamperometry curve at −0.6 V and -0.7 V, respectively, for 24 h to prove

their robustness for the practical rigors of NRR. As shown in **Figure 6 (d)** and **Figure 7 (d)**, it can be seen that the current density dropped initially to a threshold value but then attained decent stability within a relatively brief time.

We conducted Raman analysis on the C- ZrO_2-ZrN@KB and C- ZrO_2-ZrN samples before and after the NRR process (**Figure S13 (A) and Figure S13 (B)**) to detect any changes in the structure and the optical profile of the electrode, incorporating C- ZrO_2-ZrN@KB and C- ZrO_2-ZrN, and to thereby gain insights into their overall stability. As shown in **Figure S13 (A)**, the Raman spectra for (a) ZrO_2-ZrN@KB and for (b, c) C- ZrO_2-ZrN@KB both before and after NRR show essentially identical Raman shifts. The major peaks corresponding to the ZrO_2 and KB species (as described in **Figure S7 (a)**, **section 3.1**) remained intact before and after the NRR process. Similarly, the Raman spectra for (a) ZrO_2-ZrN and for (b, c) C- ZrO_2-ZrN both before and after NRR also effectively demonstrate the same Raman shifts, while the main peaks corresponding to the ZrN (as described in **Figure S7 (b)**, **section 3.1**) also stayed constant within error, before and after the NRR process. The enhanced carbon signals in C- ZrO_2-ZrN@KB and C- ZrO_2-ZrN before and after NRR can be attributed to the carbon paper.

These aggregate observations suggest that the C- ZrO_2-ZrN@KB and C- ZrO_2-ZrN electrodes were sufficiently robust enough to withstand the NRR electrolysis conditions, involving not only a strong acid medium but also constant charging−discharging processes. Subsequently, we conducted recycling tests for five consecutive NRR cycles at −0.7 V for 3 h for ZrO_2-ZrN and ended up re-using the same C- ZrO_2-ZrN electrode for all of the electrocatalytic cycles, while keeping other reaction parameters intact. The results were obtained by use of the indophenol method and are presented in **Figure 8 (a)** and **Figure 8 (b).** An exceedingly small difference in the measured V_{NH3} and FE values was observed between each test (**Figure 8 (a)**).

The outstanding observed recyclability of the catalyst until the fifth cycle can be ascribed to the excellent durability and stability of C- ZrO_2-ZrN. To ensure that the morphology, composition, and performance of the catalyst ZrO_2-ZrN can remain relatively stable after the catalyst stability test, we have conducted the XRD and SEM-EDS analysis of the used catalyst as shown in **Figure S14** and **Figure S15**, respectively. The XRD of the used ZrO_2-ZrN catalyst showed peaks corresponding to the planes of ZrN and ZrO_2 similar to that of the fresh catalyst shown in **Figure S6(b)**, indicating the catalyst remained intact after the NRR experiment. However, an extra broad peak at 2θ value of around 17 º was observed, which is obvious due to the presence of oxidized carbon from the carbon paper.[83, 84] Similarly, the SEM-EDS of the used catalyst showed that the Zr, O, and N were well distributed even after the NRR experiments. The carbon from the carbon paper was also observed in the EDS mapping image of the used ZrO_2-ZrN. Overall, it is concluded that the ZrO_2-ZrN catalyst morphology, composition, and integrity remained intact after the stability test.

Hydrazine (N_2H_4) is the most common active intermediate, which may be released as a byproduct along with the ammonia.[85-87] Therefore, to assess its presence or absence, we also tried to detect hydrazine (N_2H_4) via the Chrisp and Watt method,[41] using the standard curve for the N_2H_4 assay. It is shown in **Figure S4** and possesses good linearity ($y = 0.2486 x + 0.0116$, $R^2 = 0.999$). As highlighted in **Figure S16**, it was found that the concentration of N_2H_4 was negligible in the resultant electrolytes at all electrolysis potentials analyzed. These data strongly suggest that both ZrO_2-ZrN@KB and ZrO_2-ZrN possess an excellent selectivity toward NH_3 production.

To further probe and verify the origin of NH_3 formation in ZrO_2-ZrN -catalyzed NRR, we recorded the ^1H NMR spectra of the NH_4^+ species contained within the electrolyte. As shown in **Figure 9 a**, the ^1H NMR analysis for NH_4Cl displayed a triplet coupling at 7.08, 6.97, and 6.87

ppm (blue curve).[25, 38] The variation in the concentrations of NH_4Cl showed a decent linear relationship with the magnitude of the ^1H NMR signals detected at 6.97 ppm. The tested sample of ZrO_2-ZrN (electrolysis at −0.7 V) highlighted a 1:1:1 triplet at 7.06, 6.95, and 6.85 ppm (red curve). The standard curve (**Figure 9 b**) suggested that the concentration of NH_4^+ in the test sample was deemed to be 0.56 μg mL^{-1}. This value was found to be in good agreement with that independently obtained from the indophenol blue method, which was measured to be 0.6 μg mL^{-1}, as shown in **Table 2**.

To verify the N source of the as-formed NH_3, we conducted the ^{15}N isotopic labeling experiment by bubbling in $^{15}N_2$ into the electrolyte to produce NH_3 by NRR. As demonstrated in **Figure 9 a**, the standard sample of $^{15}NH_4Cl$ evinced a doublet coupling at 6.99 and 6.85 ppm which was distinct from normal NH_4Cl, as noted in the ^1H NMR spectra (green curve in **Figure 9 a**). In the NRR conducted on the ZrO_2-ZrN combined electrocatalyst with the $^{15}N_2$-saturated electrolyte at −0. 7 V, peaks similar to the ^1H NMR spectra of $^{15}NH_4Cl$ were observed at 7 and 6.86 ppm.[25, 82] Hence, it can be reasonably concluded that the observed NH_3 is produced by the electrocatalytic N_2 reduction when employing ZrO_2-ZrN as the electrocatalyst.

As per the DFT studies on transition metal nitrides, such as VN, CrN, ZrN, and NbN, the catalytic activities of the rock salt, RS(100/111), and the zinc blende, ZB(100/110), structures for reducing N_2 to NH_3 were found to be energetically promising on the surface of nitrides.[27, 88] As mentioned in previous literature, the catalytic cycle for the formation of $2NH_3$ could be sustained on all of the external facets of ZrN owing to the faster regeneration of the catalyst with nitrogen (replenishment of the vacancy) as opposed to the migration of the nitrogen into the surface (decomposition).[27, 88] Hence, based on the previous studies, we have proposed a mechanism for the electrochemical routes for NRR on the Zr-N surface of the ZrO_2-ZrN electrocatalyst.[88-92]

The proposed mechanism is highlighted in **Figure 10**. Since the N atoms are known to protrude slightly from the surface and are thus more exposed than the metal atoms, it is apparent that the most favorable H adsorption site is at the outer surface of the electrocatalyst. In the mechanism then, it is postulated that first, the protonation of the nitrogen atom occurs on the surface, and after the formation of the first NH_3 molecule, an N vacancy is created. This vacancy is then replenished by the adsorption of a solvated N_2 molecule from the electrolyte, wherein one of the N atoms is used to fill up the N vacancy, and the additional N atom becomes further hydrogenated to release a second NH_3 molecule. However, it is difficult to state here whether the mechanism is "dissociative" or "associative." Specifically, it is ambiguous as to whether the adsorbed N_2 initially dissociates without protonation or the adsorbed N_2 is protonated prior to dissociation. This nuance is difficult to differentiate, given the complex composition of the electrocatalyst, which incorporates ZrN, ZrO_2, and ZrON within the structure.[27, 88, 93]

4. Conclusions

In summary, we have studied the electrocatalytic activity of two ZrO_2-ZrN-based nanocatalysts for NRR. Specifically, the two nanocatalysts used for NRR were synthesized through nitriding Zr, either in the presence or absence of KB, respectively. Both of these as-prepared catalysts incorporated a combination of tetragonal ZrO_2, ZrON, and cubic ZrN. In the presence of KB, the as-obtained nanocatalyst highlighted ZrO_2 as the majority phase, while in the absence of KB, ZrN was the predominant species. Between these two catalysts, it was found that ZrO_2-ZrN achieved the highest V_{NH3} of 84.1 μg h^{-1} mg^{-1} at -0.7 V and a correspondingly high FE of 21.2 % at −0.6 V vs. RHE in an acidic solution. The enhanced activity of ZrO_2-ZrN

can in principle be attributed to the accessibility of readily available active ZrN sites at the center of the material with the ZrO_2 localized on the outer shell.

To the best of our knowledge, the NRR performance metrics of the ZrO_2-ZrN@KB and ZrO_2-ZrN nanocatalysts are superior to or comparable to that of most of the recently reported metal-nitride electrocatalysts. We speculate that the activity of the ZrN–based electrocatalyst towards NRR performance could be enhanced by further increasing the number of available active ZrN sites through other possible synthetic strategies, such as but not limited to the use of an inert atmosphere in the synthesis process, control over reaction temperatures, and regulation of the dwell time.

Author Contribution: Mitu Sharma: Methodology, Conceptualization, Validation, Investigation, Data collection, Visualization, Writing – review & editing**. Kotaro Sasaki:** Conceptualization, Methodology. **Gary Halada:** XPS data collection and XPS discussion. **Krishnakumari Pamula:** Collection of Raman data. **Tae Jin Kim:** Raman analysis discussion. **Stanislaus S. Wong:** Supervision, Resources, Project administration, Funding acquisition, Conceptualization, Validation, Writing – original draft.

Supporting Information: Electrocatalytic experiment setup photograph, chemical reactions, NH_4Cl and hydrazine calibration curves, characterization data of the samples, including size distribution, XRD, Raman, and XPS, all LSV curves, nitrate reduction reaction chronoamperometric, and indophenol UV-vis curve, NRR activity comparison table, time-dependent study results, used catalyst characterization using Raman, XRD, and SEM-EDS, all hydrazine test plots.

Acknowledgments: The experiments in this work were financially supported by seed grant funding through the Office of the Vice President for Research at Stony Brook University. The

authors thank Fernando Camino and Kim Kisslinger for their assistance with HRTEM data collection at the Center for Functional Nanomaterials located in Brookhaven National Laboratory (BNL) which is supported by the U.S. Department of Energy under Contract No. DE-SC0012704. We acknowledge James Anselmini and Nicholas Camillone from the Chemistry Department at Brookhaven National Laboratory for providing valuable suggestions and setting up the $^{15}N_2$ isotopic labeling experiment. We also thank Francis Picart from the Department of Chemistry at Stony Brook University for his assistance with the setup of the NMR experiments. The catalytic activity measurements were supported by the Division of Chemical Science, Geosciences, and Bioscience of the Office of Basic Energy Sciences at the U.S. Department of Energy (DOE) under Contract No DE-SC0012704.

References –

(1) Fowler, D.; Coyle, M.; Skiba, U.; Sutton, M. A.; Cape, J. N.; Reis, S.; Sheppard, L. J.; Jenkins, A.; Grizzetti, B.; Galloway, J. N. The global nitrogen cycle in the twenty-first century. *Philosophical Transactions of the Royal Society B: Biological Sciences* **2013**, *368* (1621), 20130164.
(2) MacFarlane, D. R.; Choi, J.; Suryanto, B. H.; Jalili, R.; Chatti, M.; Azofra, L. M.; Simonov, A. N. Liquefied sunshine: Transforming renewables into fertilizers and energy carriers with electromaterials. *Advanced Materials* **2020**, *32* (18), 1904804.
(3) Du, H.-L.; Chatti, M.; Hodgetts, R. Y.; Cherepanov, P. V.; Nguyen, C. K.; Matuszek, K.; MacFarlane, D. R.; Simonov, A. N. Electroreduction of nitrogen with almost 100% current-to-ammonia efficiency. *Nature* **2022**, *609* (7928), 722-727.
(4) Yao, D.; Tang, C.; Li, L.; Xia, B.; Vasileff, A.; Jin, H.; Zhang, Y.; Qiao, S. Z. In situ fragmented bismuth nanoparticles for electrocatalytic nitrogen reduction. *Advanced Energy Materials* **2020**, *10* (33), 2001289.
(5) Chen, S.; Lian, K.; Liu, W.; Liu, Q.; Qi, G.; Luo, J.; Liu, X. Engineering active sites of cathodic materials for high-performance Zn-nitrogen batteries. *Nano Research* **2023**, *16* (7), 9214-9230.
(6) Yang, M.; Wei, T.; He, J.; Liu, Q.; Feng, L.; Li, H.; Luo, J.; Liu, X. Au nanoclusters anchored on TiO_2 nanosheets for high-efficiency electroreduction of nitrate to ammonia. *Nano Research* **2024**, *17* (3), 1209-1216.
(7) Martín, A. J.; Shinagawa, T.; Pérez-Ramírez, J. Electrocatalytic reduction of nitrogen: from Haber-Bosch to ammonia artificial leaf. *Chem* **2019**, *5* (2), 263-283.
(8) Martín, A. J.; Veenstra, F. L.; Lüthi, J.; Verel, R.; Pérez-Ramírez, J. Toward reliable and accessible ammonia quantification in the electrocatalytic reduction of nitrogen. *Chem Catalysis* **2021**, *1* (7), 1505-1518.
(9) Cui, X.; Tang, C.; Zhang, Q. A review of electrocatalytic reduction of dinitrogen to ammonia under ambient conditions. *Advanced Energy Materials* **2018**, *8* (22), 1800369.
(10) Qing, G.; Ghazfar, R.; Jackowski, S. T.; Habibzadeh, F.; Ashtiani, M. M.; Chen, C.-P.; Smith III, M. R.; Hamann, T. W. Recent advances and challenges of electrocatalytic N_2 reduction to ammonia. *Chemical reviews* **2020**, *120* (12), 5437-5516.
(11) Van der Ham, C. J.; Koper, M. T.; Hetterscheid, D. G. Challenges in reduction of dinitrogen by proton and electron transfer. *Chemical Society Reviews* **2014**, *43* (15), 5183-5191.
(12) Guo, X.; Gu, J.; Lin, S.; Zhang, S.; Chen, Z.; Huang, S. Tackling the activity and selectivity challenges of electrocatalysts toward the nitrogen reduction reaction via atomically dispersed biatom catalysts. *Journal of the American Chemical Society* **2020**, *142* (12), 5709-5721.
(13) Jia, H.-P.; Quadrelli, E. A. Mechanistic aspects of dinitrogen cleavage and hydrogenation to produce ammonia in catalysis and organometallic chemistry: relevance of metal hydride bonds and dihydrogen. *Chemical Society Reviews* **2014**, *43* (2), 547-564.
(14) Lv, C.; Qian, Y.; Yan, C.; Ding, Y.; Liu, Y.; Chen, G.; Yu, G. Defect engineering metal-free polymeric carbon nitride electrocatalyst for effective nitrogen fixation under ambient conditions. *Angewandte Chemie* **2018**, *130* (32), 10403-10407.
(15) Seh, Z. W.; Kibsgaard, J.; Dickens, C. F.; Chorkendorff, I.; Nørskov, J. K.; Jaramillo, T. F. Combining theory and experiment in electrocatalysis: Insights into materials design. *Science* **2017**, *355* (6321), eaad4998.
(16) Guo, C.; Ran, J.; Vasileff, A.; Qiao, S.-Z. Rational design of electrocatalysts and photo (electro) catalysts for nitrogen reduction to ammonia (NH 3) under ambient conditions. *Energy & Environmental Science* **2018**, *11* (1), 45-56.
(17) Zhang, H.; He, X.; Dong, K.; Yao, Y.; Sun, S.; Zhang, M.; Yue, M.; Yang, C.; Zheng, D.; Liu, Q. Selenate promoted stability improvement of nickel selenide nanosheet array with an amorphous NiOOH layer for seawater oxidation. *Materials Today Physics* **2023**, *38*, 101249.

(18) Yang, X.; Niu, M.; Ma, H.; Zhang, H.; Zhang, W.; Ji, X. Enhancement of alkaline water-oxidation activity for amorphous CoOx by the underlying remote-region atom seeding. *International Journal of Hydrogen Energy* **2024**, *74*, 338-345.
(19) Mu, Y.; Ma, R.; Xue, S.; Shang, H.; Lu, W.; Jiao, L. Recent advances and perspective on transition metal heterogeneous catalysts for efficient electrochemical water splitting. *Carbon Neutralization* **2024**, *3* (1), 4-31.
(20) Xu, X.; Guo, K.; Sun, J.; Yu, X.; Miao, X.; Lu, W.; Jiao, L. Interface Engineering of Mo-doped Ni_2P/Fe_xP-V Multiheterostructure for Efficient Dual-pH Hydrogen Evolution and Overall Water Splitting. *Advanced Functional Materials* **2024**, 2400397.
(21) Wu, X.; Xia, L.; Wang, Y.; Lu, W.; Liu, Q.; Shi, X.; Sun, X. Mn_3O_4 nanocube: an efficient electrocatalyst toward artificial N_2 fixation to NH_3. *Small* **2018**, *14* (48), 1803111.
(22) Yang, X.; Ling, F.; Su, J.; Zi, X.; Zhang, H.; Zhang, H.; Li, J.; Zhou, M.; Wang, Y. Insights into the role of cation vacancy for significantly enhanced electrochemical nitrogen reduction. *Applied Catalysis B: Environmental* **2020**, *264*, 118477.
(23) Yang, X.; Wan, J.; Zhang, H.; Wang, Y. In situ modification of the d-band in the core–shell structure for efficient hydrogen storage via electrocatalytic N_2 fixation. *Chemical Science* **2022**, *13* (37), 11030-11037.
(24) Luo, S.; Li, X.; Wang, M.; Zhang, X.; Gao, W.; Su, S.; Liu, G.; Luo, M. Long-term electrocatalytic N_2 fixation by MOF-derived Y-stabilized ZrO_2: insight into the deactivation mechanism. *Journal of Materials Chemistry A* **2020**, *8* (11), 5647-5654.
(25) Dong, S.; Xia, J.; Zhu, H.; Du, X.; Gu, Y.; Liu, Q.; Luo, Y.; Kong, Q.; Guo, H.; Li, T. ZrO_2/C Nanosphere Enables High-Efficiency Nitrogen Reduction to Ammonia at Ambient Conditions. *ChemCatChem* **2022**, *14* (17), e202200458.
(26) Yang, X.; Nash, J.; Anibal, J.; Dunwell, M.; Kattel, S.; Stavitski, E.; Attenkofer, K.; Chen, J. G.; Yan, Y.; Xu, B. Mechanistic insights into electrochemical nitrogen reduction reaction on vanadium nitride nanoparticles. *Journal of the American Chemical Society* **2018**, *140* (41), 13387-13391.
(27) Abghoui, Y.; Garden, A. L.; Howalt, J. G.; Vegge, T.; Skúlason, E. Electroreduction of N_2 to ammonia at ambient conditions on mononitrides of Zr, Nb, Cr, and V: A DFT guide for experiments. *Acs Catalysis* **2016**, *6* (2), 635-646.
(28) Abghoui, Y.; Skúlason, E. Onset potentials for different reaction mechanisms of nitrogen activation to ammonia on transition metal nitride electro-catalysts. *Catalysis Today* **2017**, *286*, 69-77.
(29) Abghoui, Y.; Skúlasson, E. Transition metal nitride catalysts for electrochemical reduction of nitrogen to ammonia at ambient conditions. *Procedia Computer Science* **2015**, *51*, 1897-1906.
(30) Banerjee, A.; Ceballos, B. M.; Kreller, C.; Mukundan, R.; Pilania, G. A first-principles investigation of nitrogen reduction to ammonia on zirconium nitride and oxynitride surfaces. *Journal of Materials Science* **2022**, *57* (22), 10213-10224.
(31) Wu, J.; Yang, L.; Liu, X.; Zhang, Z.; Liu, S.; Xiao, B. ZrN_6-Doped Graphene for Ammonia Synthesis: A Density Functional Theory Study. *ChemPhysChem* **2023**, e202200864.
(32) Pickett, C. J.; Talarmin, J. Electrosynthesis of ammonia. *Nature* **1985**, *317* (6038), 652-653.
(33) Abghoui, Y.; Garden, A. L.; Hlynsson, V. F.; Björgvinsdóttir, S.; Ólafsdóttir, H.; Skúlason, E. Enabling electrochemical reduction of nitrogen to ammonia at ambient conditions through rational catalyst design. *Physical Chemistry Chemical Physics* **2015**, *17* (7), 4909-4918.
(34) Zhang, R.; Zhang, Y.; Ren, X.; Cui, G.; Asiri, A. M.; Zheng, B.; Sun, X. High-efficiency electrosynthesis of ammonia with high selectivity under ambient conditions enabled by VN nanosheet array. *ACS sustainable chemistry & engineering* **2018**, *6* (8), 9545-9549.
(35) Zhang, X.; Kong, R.-M.; Du, H.; Xia, L.; Qu, F. Highly efficient electrochemical ammonia synthesis via nitrogen reduction reactions on a VN nanowire array under ambient conditions. *Chemical communications* **2018**, *54* (42), 5323-5325.

(36) Cui, M.; Zhang, T.; Wang, M.; Xu, W.; Zhang, Y.; Song, P.; Wang, C.; Yang, Y.; Zhang, X.; Fan, X. Chemically anchoring molybdenum atoms onto micropore-rich VN nanosheet for boosted nitrogen electro-fixation via hydrogen bonds. *Chemical Engineering Journal* **2022**, *446*, 136915.
(37) Fu, B.; Gao, L. Synthesis of nanocrystalline zirconium nitride powders by reduction–nitridation of zirconium oxide. *Journal of the American Ceramic Society* **2004**, *87* (4), 696-698.
(38) Liu, Z.; Zhang, M.; Wang, H.; Cang, D.; Ji, X.; Liu, B.; Yang, W.; Li, D.; Liu, J. Defective carbon-doped boron nitride nanosheets for highly efficient electrocatalytic conversion of N_2 to NH_3. *ACS sustainable chemistry & engineering* **2020**, *8* (13), 5278-5286.
(39) Zhang, Y.; Du, H.; Ma, Y.; Ji, L.; Guo, H.; Tian, Z.; Chen, H.; Huang, H.; Cui, G.; Asiri, A. M. Hexagonal boron nitride nanosheet for effective ambient N_2 fixation to NH_3. *Nano Research* **2019**, *12*, 919-924.
(40) Zhu, D.; Zhang, L.; Ruther, R. E.; Hamers, R. J. Photo-illuminated diamond as a solid-state source of solvated electrons in water for nitrogen reduction. *Nature materials* **2013**, *12* (9), 836-841.
(41) Watt, G. W.; Chrisp, J. D. Spectrophotometric method for determination of hydrazine. *Analytical Chemistry* **1952**, *24* (12), 2006-2008.
(42) Zhang, Y.; Dong, H.; Zhang, H.; Liu, Y.; Ji, M.; Xu, Y.; Wang, Q.; Luo, L. $Li_4Ti_5O_{12}$/Ketjen Black with open conductive frameworks for high-performance lithium-ion batteries. *Electrochimica Acta* **2016**, *201*, 179-186.
(43) Fu, X.; Lu, Y.; Peng, Y. An integrated electrochemical immunosensor based on Pd–Ir cubic nanozyme and Ketjen black for ultrasensitive detection of circulating tumor cells. *Analytical Biochemistry* **2024**, *686*, 115428.
(44) Yun, Y. S.; Shim, J.; Tak, Y.; Jin, H.-J. Nitrogen-enriched multimodal porous carbons for supercapacitors, fabricated from inclusion complexes hosted by urea hydrates. *RSC advances* **2012**, *2* (10), 4353-4358.
(45) Jameson, A.; Gyenge, E. High Activity Carbonaceous Electrodes for Zinc-Iodine Flow Batteries. *Available at SSRN 4593886*.
(46) Meng, T.; Ara, M.; Wang, L.; Naik, R.; Ng, K. S. Enhanced capacity for lithium–air batteries using $LaFe_{0.5}Mn_{0.5}O_3$–CeO_2 composite catalyst. *Journal of Materials Science* **2014**, *49*, 4058-4066.
(47) Chisaka, M.; Ishihara, A.; Morioka, H.; Nagai, T.; Yin, S.; Ohgi, Y.; Matsuzawa, K.; Mitsushima, S.; Ota, K.-i. Zirconium oxynitride-catalyzed oxygen reduction reaction at polymer electrolyte fuel cell cathodes. *ACS omega* **2017**, *2* (2), 678-684.
(48) Dey, S.; Roy, S. N.; Majumdar, S.; Ghosh, S.; Sahoo, G. C. Dispersion study of zirconia nano-powders using dolapix CE64 and M65 dispersant to develop UF membrane over novel clay-alumina based ceramic support for water treatment. *Transactions of the Indian Ceramic Society* **2019**, *78* (4), 187-194.
(49) Lam, D. V.; Suematsu, H.; Ogawa, T. Characterization of ZrN, ZrO_2 and β'–$Zr_7O_{11}N_2$ nanoparticles synthesized by pulsed wire discharge. *Journal of the American Ceramic Society* **2017**, *100* (10), 4884-4892.
(50) Zhao, S.; Ma, J.; Xu, R.; Lin, X.; Cheng, X.; Hao, S.; Zhao, X.; Deng, C.; Liu, B. Synthesis and characterization of zirconium nitride nanopowders by internal gelation and carbothermic nitridation. *Scientific reports* **2019**, *9* (1), 19199.
(51) Yuan, Y.; Wang, J.; Adimi, S.; Shen, H.; Thomas, T.; Ma, R.; Attfield, J. P.; Yang, M. Zirconium nitride catalysts surpass platinum for oxygen reduction. *Nature materials* **2020**, *19* (3), 282-286.
(52) Zhang, P.; Choy, K.-L. The synthesis of single tetragonal phase zirconia by sol-gel route. *Int. J. Eng. Res. Sci* **2015**, *1*, 18-24.
(53) Kumar, D.; Singh, A.; Kaur, N.; Thakur, A.; Kaur, R. Tailoring structural and optical properties of ZrO_2 with nickel doping. *SN Applied Sciences* **2020**, *2*, 1-8.
(54) Rizzo, A.; Signore, M.; Mirenghi, L.; Piscopiello, E.; Tapfer, L. Physical properties evolution of sputtered zirconium oxynitride films: effects of the growth temperature. *Journal of Physics D: Applied Physics* **2009**, *42* (23), 235401.
(55) Reddy, C. V.; Babu, B.; Reddy, I. N.; Shim, J. Synthesis and characterization of pure tetragonal ZrO_2 nanoparticles with enhanced photocatalytic activity. *Ceramics International* **2018**, *44* (6), 6940-6948.

(56) Salah, N.; Habib, S. S.; Khan, Z. H.; Djouider, F. Thermoluminescence and photoluminescence of ZrO_2 nanoparticles. *Radiation Physics and Chemistry* **2011**, *80* (9), 923-928.
(57) Chen, N.; Guo, M.; Zhao, F.; Yin, W.; Wang, J.; Wang, Q.; Wang, C. Feasibility of Biological Applications for Zirconium Nitride Powders Synthesized by Gas–Solid Elemental Combination Method. *Journal of Nanoscience and Nanotechnology* **2019**, *19* (6), 3319-3325.
(58) do Rego, U. A.; Sgarbi, R.; Lopes, T.; dos Santos, C. C.; Tanaka, A. A.; Ticianelli, E. A. Effect of substrate and pyrolysis atmosphere of FeNx materials on electrocatalysis of the oxygen reduction reaction. *Electrocatalysis* **2021**, *12* (5), 548-563.
(59) Ungar, T.; Gubicza, J.; Ribarik, G.; Pantea, C.; Zerda, T. W. Microstructure of carbon blacks determined by X-ray diffraction profile analysis. *Carbon* **2002**, *40* (6), 929-937.
(60) Rizzo, A.; Valerini, D.; Capodieci, L.; Mirenghi, L.; Di Benedetto, F.; Protopapa, M. Reactive bipolar pulsed dual magnetron sputtering of ZrN films: The effect of duty cycle. *Applied Surface Science* **2018**, *427*, 994-1002.
(61) Chen, L.; Mashimo, T.; Omurzak, E.; Okudera, H.; Iwamoto, C.; Yoshiasa, A. Pure tetragonal ZrO_2 nanoparticles synthesized by pulsed plasma in liquid. *The Journal of Physical Chemistry C* **2011**, *115* (19), 9370-9375.
(62) Wong, Y. H.; Cheong, K. Y. Properties of thermally oxidized and nitrided Zr-oxynitride thin film on 4H–SiC in diluted N_2O ambient. *Materials Chemistry and Physics* **2012**, *136* (2-3), 624-637.
(63) Basahel, S. N.; Ali, T. T.; Mokhtar, M.; Narasimharao, K. Influence of crystal structure of nanosized ZrO_2 on photocatalytic degradation of methyl orange. *Nanoscale research letters* **2015**, *10*, 1-13.
(64) Ciszak, C.; Mermoux, M.; Gutierrez, G.; Leprêtre, F.; Duriez, C.; Popa, I.; Fayette, L.; Chevalier, S. Raman spectra analysis of ZrO_2 thermally grown on Zircaloy substrates irradiated with heavy ion: Effects of oxygen isotopic substitution. *Journal of Raman Spectroscopy* **2019**, *50* (3), 425-435.
(65) Moura, C.; Carvalho, P.; Vaz, F.; Cunha, L.; Alves, E. Raman spectra and structural analysis in ZrO_xN_y thin films. *Thin Solid Films* **2006**, *515* (3), 1132-1137.
(66) Cassinese, A.; Iavarone, M.; Vaglio, R.; Grimsditch, M.; Uran, S. Transport properties of ZrN superconducting films. *Physical Review B* **2000**, *62* (21), 13915.
(67) Li, Y.; Guo, C.; Li, J.; Liao, W.; Li, Z.; Zhang, J.; Chen, C. Pyrolysis-induced synthesis of iron and nitrogen-containing carbon nanolayers modified graphdiyne nanostructure as a promising core-shell electrocatalyst for oxygen reduction reaction. *Carbon* **2017**, *119*, 201-210.
(68) Lackner, P.; Zou, Z.; Mayr, S.; Diebold, U.; Schmid, M. Using photoelectron spectroscopy to observe oxygen spillover to zirconia. *Physical Chemistry Chemical Physics* **2019**, *21* (32), 17613-17620.
(69) Gondal, M.; Fasasi, T.; Baig, U.; Mekki, A. Effects of oxidizing media on the composition, morphology and optical properties of colloidal zirconium oxide nanoparticles synthesized via pulsed laser ablation in liquid technique. *Journal of Nanoscience and Nanotechnology* **2018**, *18* (6), 4030-4039.
(70) Brenier, R.; Mugnier, J.; Mirica, E. XPS study of amorphous zirconium oxide films prepared by sol–gel. *Applied surface science* **1999**, *143* (1-4), 85-91.
(71) Yang, X.; Li, K.; Cheng, D.; Pang, W.-L.; Lv, J.; Chen, X.; Zang, H.-Y.; Wu, X.-L.; Tan, H.-Q.; Wang, Y.-H. Nitrogen-doped porous carbon: highly efficient trifunctional electrocatalyst for oxygen reversible catalysis and nitrogen reduction reaction. *Journal of Materials Chemistry A* **2018**, *6* (17), 7762-7769.
(72) Bourlier, Y.; Bouttemy, M.; Patard, O.; Gamarra, P.; Piotrowicz, S.; Vigneron, J.; Aubry, R.; Delage, S.; Etcheberry, A. Investigation of InAlN layers surface reactivity after thermal annealings: a complete XPS study for HEMT. *ECS Journal of Solid State Science and Technology* **2018**, *7* (6), P329.
(73) Chan, M.-H.; Wu, P.-L.; Lu, F.-H. Preparation of ZrN_xO_y films by magnetron sputtering using air as a reactive gas. *Thin Solid Films* **2010**, *518* (24), 7300-7303.
(74) Carvalho, P.; Chappé, J.-M.; Cunha, L.; Lanceros-Méndez, S.; Alpuim, P.; Vaz, F.; Alves, E.; Rousselot, C.; Espinós, J.; González-Elipe, A. Influence of the chemical and electronic structure on the electrical behavior of zirconium oxynitride films. *Journal of Applied Physics* **2008**, *103* (10).

(75) Cubillos, G.; Mendoza, M.; Alfonso, J.; Blanco, G.; Bethencourt, M. Chemical composition and microstructure of zirconium oxynitride thin layers from the surface to the substrate-coating interface. *Materials Characterization* **2017**, *131*, 450-458.
(76) Signore, M.; Rizzo, A.; Mirenghi, L.; Tagliente, M.; Cappello, A. Characterization of zirconium oxynitride films obtained by radio frequency magnetron reactive sputtering. *Thin Solid Films* **2007**, *515* (17), 6798-6804.
(77) Zhang, L.; Ji, X.; Ren, X.; Luo, Y.; Shi, X.; Asiri, A. M.; Zheng, B.; Sun, X. Efficient electrochemical N_2 reduction to NH_3 on MoN nanosheets array under ambient conditions. *ACS sustainable chemistry & engineering* **2018**, *6* (8), 9550-9554.
(78) Qiu, W.; Xie, X.-Y.; Qiu, J.; Fang, W.-H.; Liang, R.; Ren, X.; Ji, X.; Cui, G.; Asiri, A. M.; Cui, G. High-performance artificial nitrogen fixation at ambient conditions using a metal-free electrocatalyst. *Nature communications* **2018**, *9* (1), 3485.
(79) Kong, J.; Lim, A.; Yoon, C.; Jang, J. H.; Ham, H. C.; Han, J.; Nam, S.; Kim, D.; Sung, Y.-E.; Choi, J. Electrochemical synthesis of NH_3 at low temperature and atmospheric pressure using a γ-Fe_2O_3 catalyst. *ACS Sustainable Chemistry & Engineering* **2017**, *5* (11), 10986-10995.
(80) Yao, Y.; Wang, H.; Yuan, X.-z.; Li, H.; Shao, M. Electrochemical nitrogen reduction reaction on ruthenium. *ACS Energy Letters* **2019**, *4* (6), 1336-1341.
(81) Sun, C. N.; Qu, Y. B.; Wang, Z. L.; Jiang, Q. Hydrogen spillover in alkaline solutions for effective nitrogen fixation. *Chemical Engineering Journal* **2023**, *471*, 144589.
(82) Li, W.; Li, K.; Ye, Y.; Zhang, S.; Liu, Y.; Wang, G.; Liang, C.; Zhang, H.; Zhao, H. Efficient electrocatalytic nitrogen reduction to ammonia with aqueous silver nanodots. *Communications Chemistry* **2021**, *4* (1), 10.
(83) Gascho, J. L.; Costa, S. F.; Recco, A. A.; Pezzin, S. H. Graphene oxide films obtained by vacuum filtration: X-ray diffraction evidence of crystalline reorganization. *Journal of Nanomaterials* **2019**, *2019* (1), 5963148.
(84) Lu, Y.; Wang, T.; Tian, Z.; Ye, Q. Preparation of graphene oxide paper as an electrode for lithium-ion batteries based on a vacuum filtration method. *International Journal of Electrochemical Science* **2017**, *12* (10), 8944-8952.
(85) Chalkley, M. J.; Drover, M. W.; Peters, J. C. Catalytic N_2-to-NH_3 (or-N_2H_4) conversion by well-defined molecular coordination complexes. *Chemical reviews* **2020**, *120* (12), 5582-5636.
(86) Wu, J.; Wang, S.; Ji, R.; Kai, D.; Kong, J.; Liu, S.; Thitsartarn, W.; Tan, B. H.; Chua, M. H.; Xu, J. In situ characterization techniques for electrochemical nitrogen reduction reaction. *ACS nano* **2024**, *18* (32), 20934-20956.
(87) Liu, R.; Fei, H.; Wang, J.; Guo, T.; Liu, F.; Wu, Z.; Wang, D. Unveiling the synergistic effect between the metallic phase and bridging S species over MoS_2 for highly efficient nitrogen fixation. *Applied Catalysis B: Environmental* **2024**, *343*, 123469.
(88) Wu, B.; Lin, Y.; Wang, X.; Chen, L. Recent advances on electrocatalytic fixation of nitrogen under ambient conditions. *Materials Chemistry Frontiers* **2021**, *5* (15), 5516-5533.
(89) Shetty, A. U.; Sankannavar, R. Exploring nitrogen reduction reaction mechanisms in electrocatalytic ammonia synthesis: a comprehensive review. *Journal of Energy Chemistry* **2024**.
(90) Iqbal, A.; Skulason, E.; Abghoui, Y. Electrochemical Nitrogen Reduction to Ammonia at Ambient Condition on the (111) Facets of Transition Metal Carbonitrides. *ChemPhysChem* **2024**, e202300991.
(91) Iqbal, A.; Skúlason, E.; Abghoui, Y. Catalytic Nitrogen Reduction on the Transition Metal Carbonitride (110) Facet: DFT Predictions and Mechanistic Insights. *The Journal of Physical Chemistry C* **2024**.
(92) Cui, L.; Sun, Z.; Wang, Y.; Jian, X.; Li, H.; Zhang, X.; Gao, X.; Li, R.; Liu, J. *H migration-assisted MvK mechanism for efficient electrochemical NH_3 synthesis over TM–TiNO. *Physical Chemistry Chemical Physics* **2024**, *26* (21), 15705-15716.
(93) Yao, Y.; Zhu, S.; Wang, H.; Li, H.; Shao, M. A spectroscopic study on the nitrogen electrochemical reduction reaction on gold and platinum surfaces. *Journal of the American Chemical Society* **2018**, *140* (4), 1496-1501.

Table of Contents Figure:

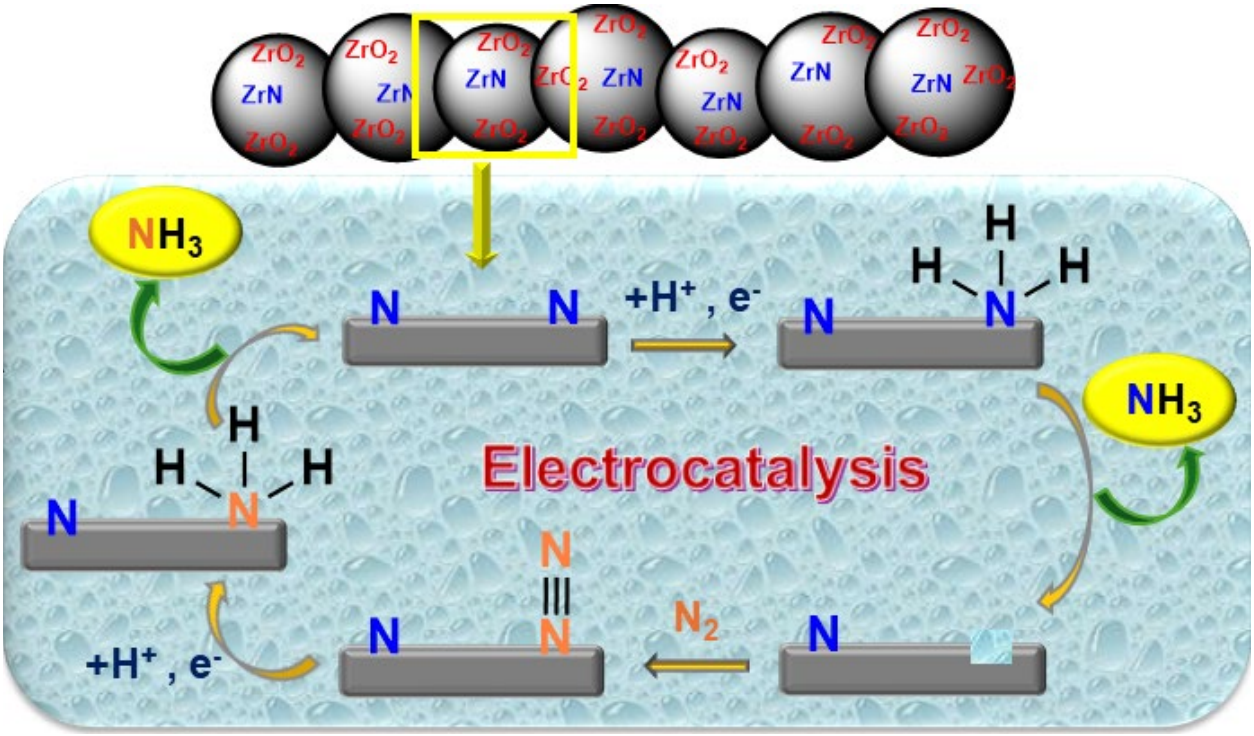

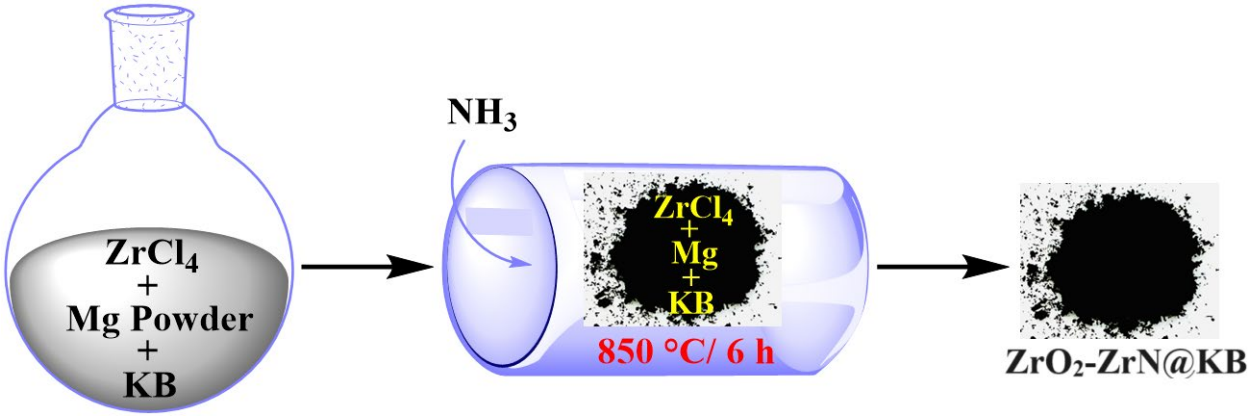

Figure 1. Schematic illustration for the stepwise synthesis of ZrO_2-ZrN@KB.

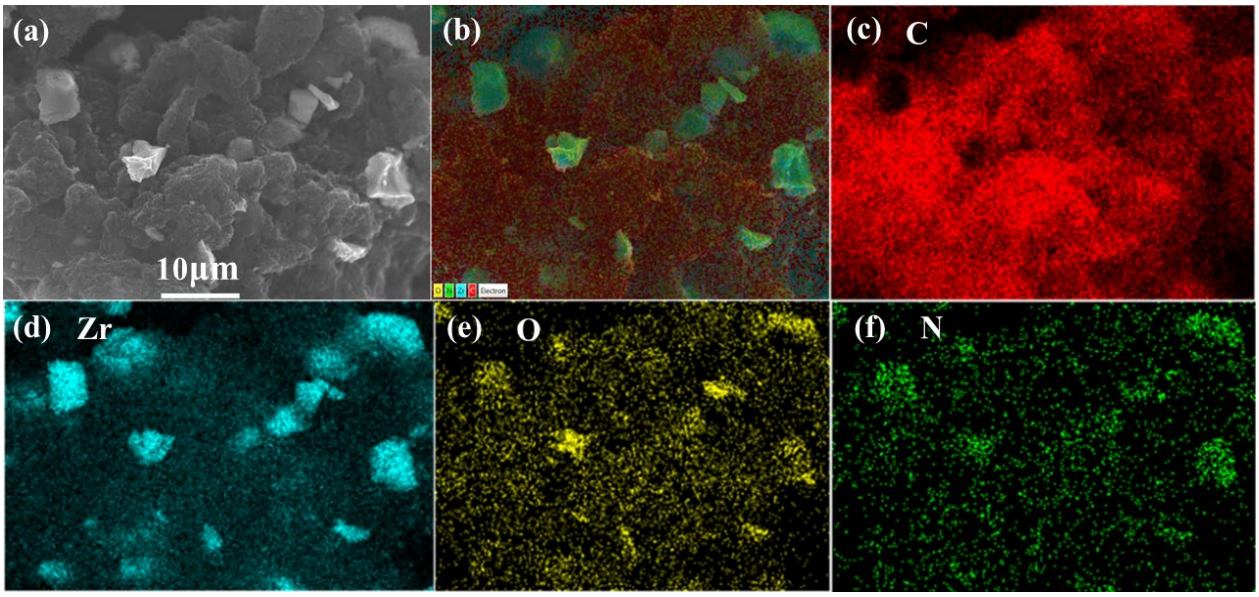

Figure 2. (a) SEM image of ZrO_2-ZrN@KB along with (b) overlap of the EDS mapping signals of the chemical elemental distribution, present within the sample. False color images of (c) carbon, (d) zirconium, (e) oxygen, and (f) nitrogen are shown.

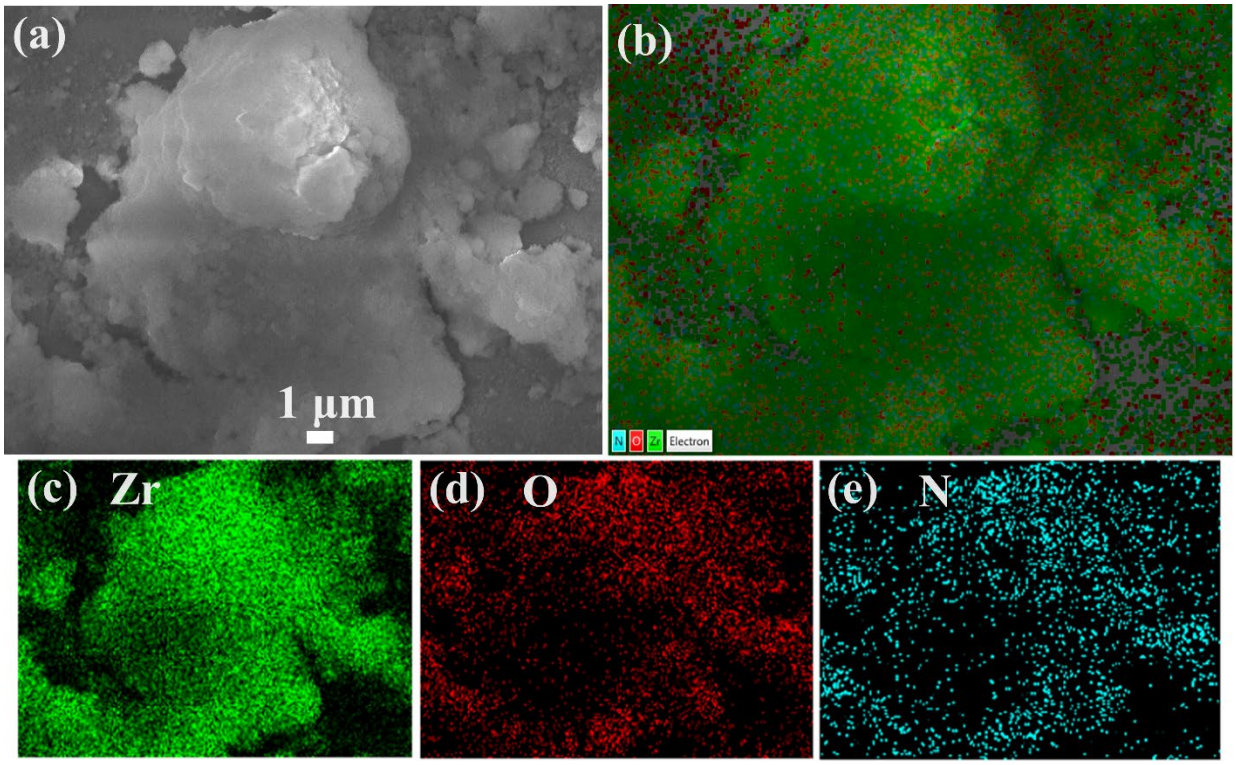

Figure 3. (a) SEM image of ZrO_2-ZrN along with (b) overlap of the EDS mapping signals of the chemical elemental distribution, present within the sample. False color images of (c) zirconium, (d) oxygen, and (e) nitrogen are shown.

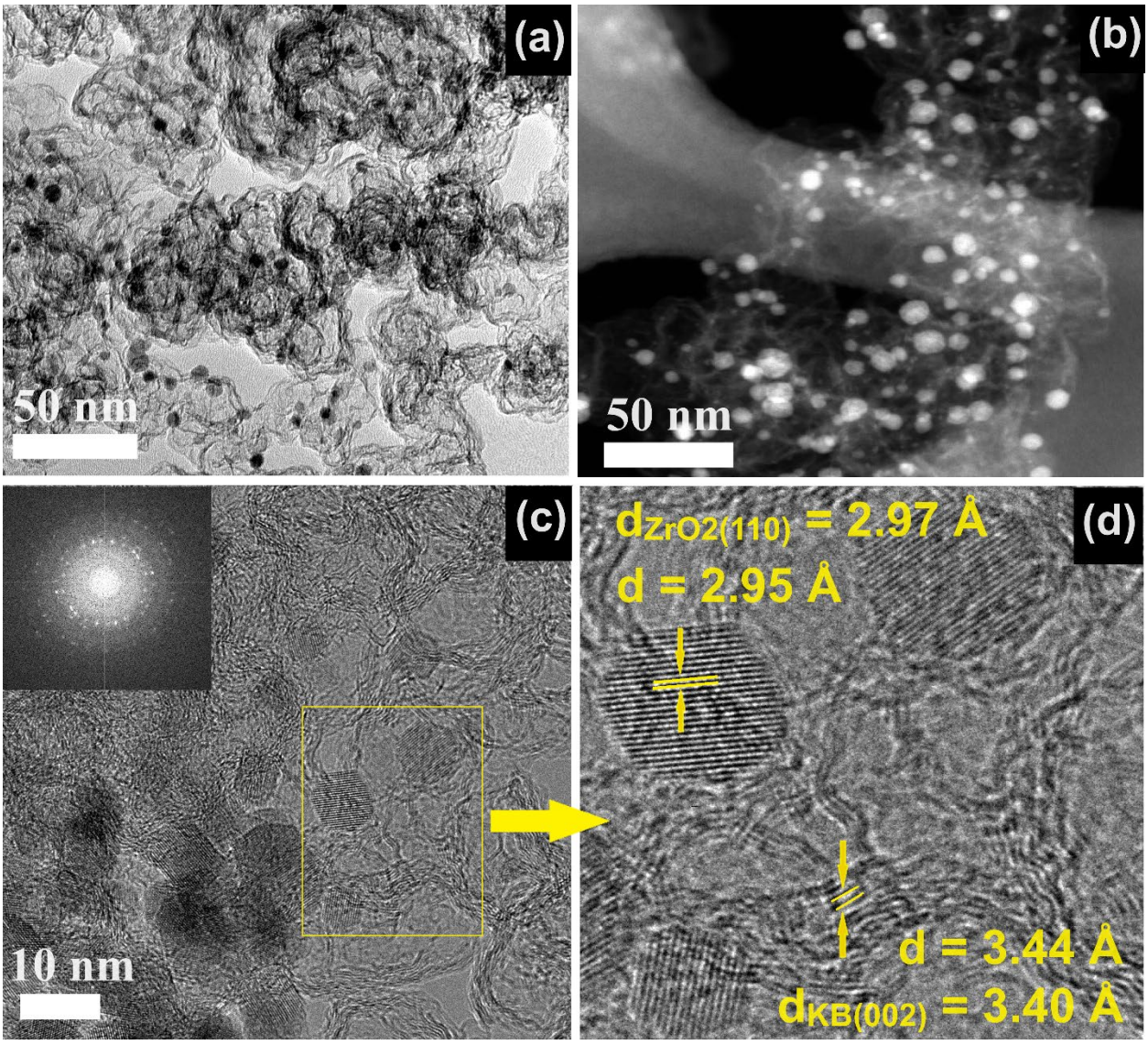

-

Figure 4. (a) TEM images of ZrO_2-ZrN@KB are presented, along with the associated (b) STEM, and (c) HRTEM with the inset highlighting the corresponding electron diffraction pattern. (d) Additional HRTEM image of the selected region of the particle, shown in (c). Lattice fringes are visible with *d* spacings of 2.97 Å and 3.44Å, ascribed to the (110) plane of tetrahedral ZrO_2 and (002) plane of KB, respectively.

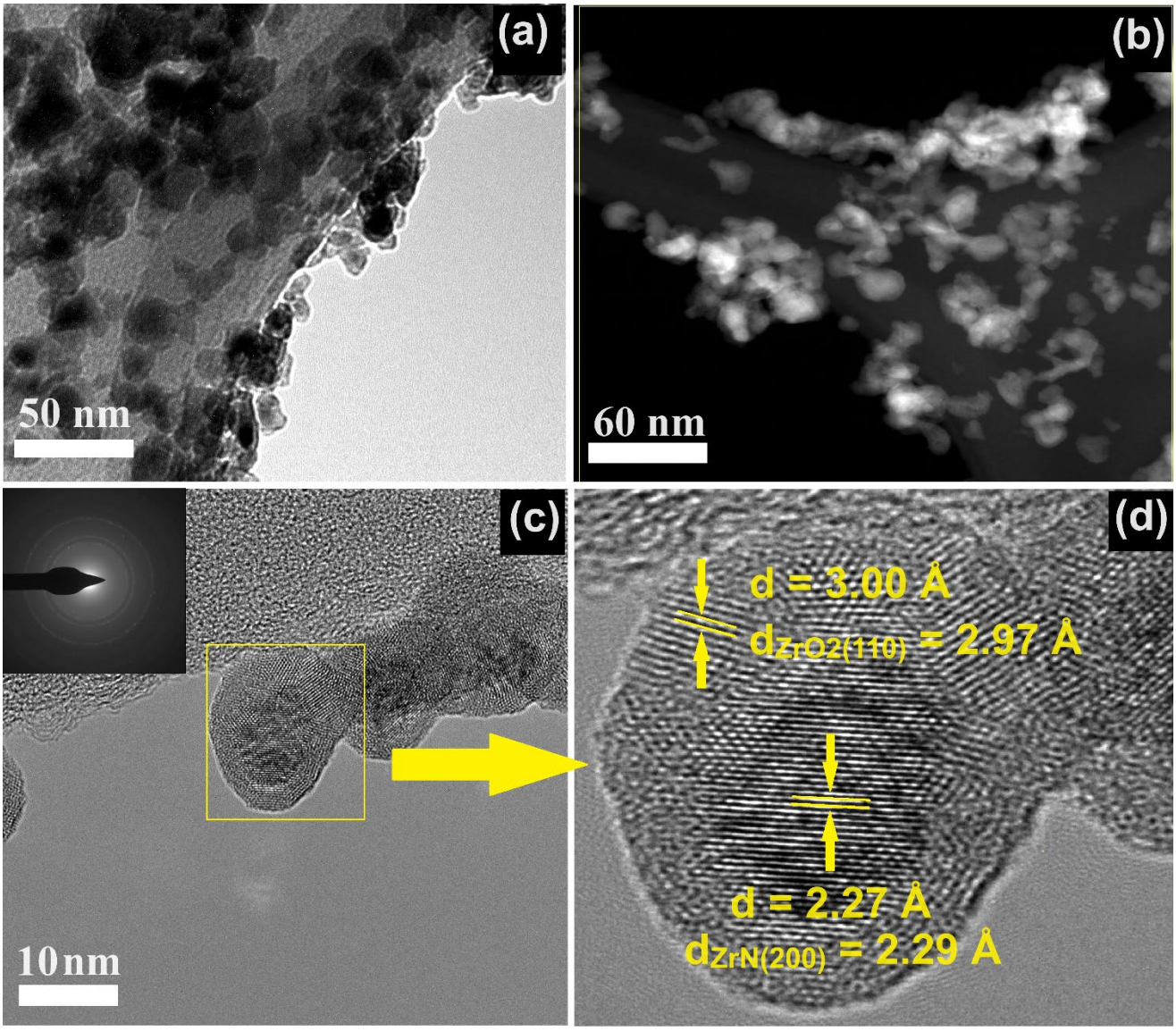

Figure 5. (a) TEM images of ZrO_2-ZrN are provided, along with the associated (b) STEM, and (c) HRTEM with the inset highlighting the corresponding electron diffraction pattern. (d) Additional HRTEM image of the selected region of the particle, shown in (c). Lattice fringes are visible with measured *d* spacings of 2.27 Å and 3.00Å, corresponding to the (200) cubic plane of ZrN and the (110) plane of tetrahedral ZrO_2.

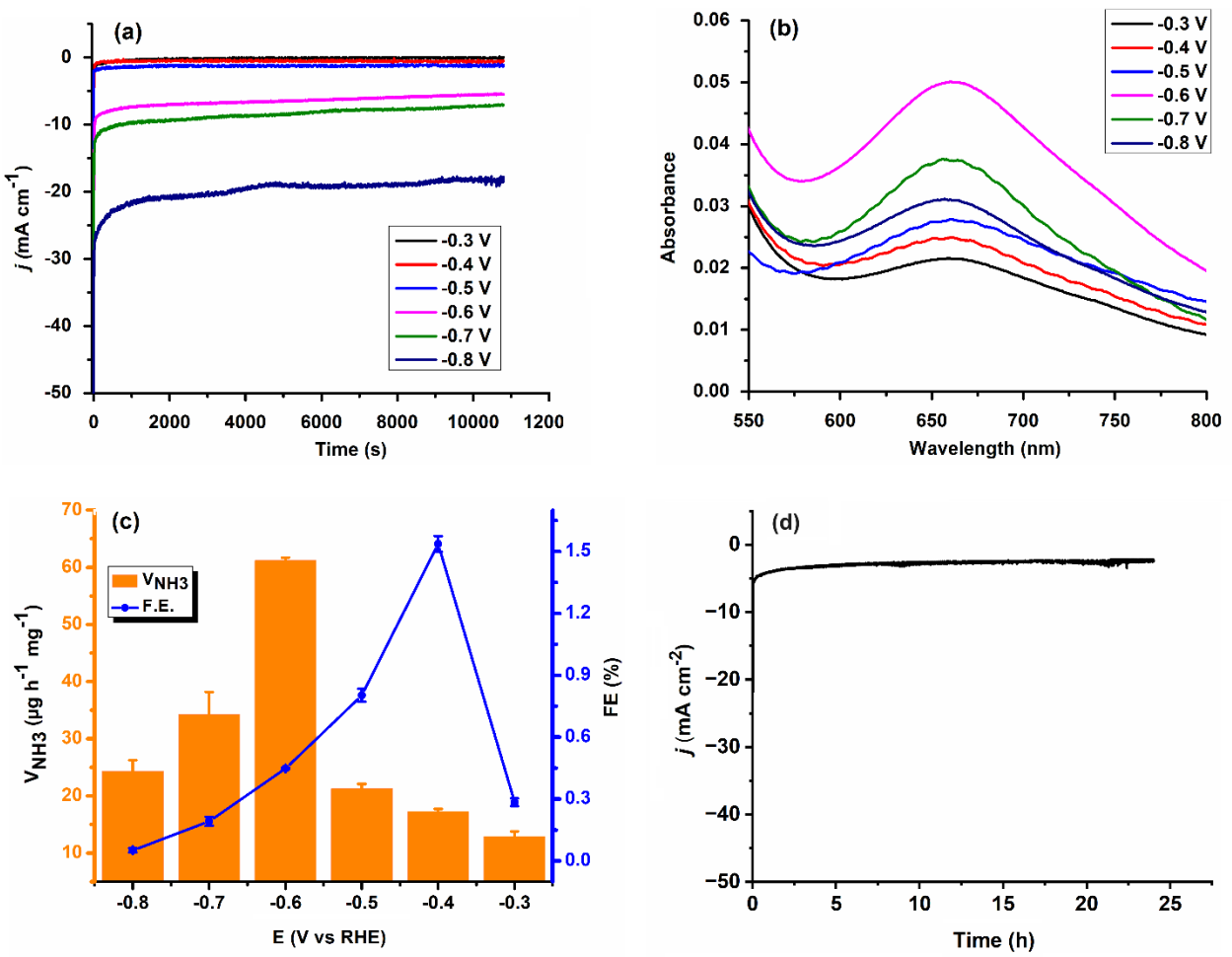

Figure 6. (a) Chronoamperometry results associated with C- ZrO_2-ZrN@KB, collected at various potentials. (b) UV−visible absorption curves of the electrolytes using the indophenol method are shown after 3 h of electrolysis, measured against different potentials. (c) V_{NH3} and FEs for C- ZrO_2-ZrN@KB are provided at each given potential. (d) Chronoamperometry results associated with C- ZrO_2-ZrN@KB were obtained at −0.6 V for 24 h.

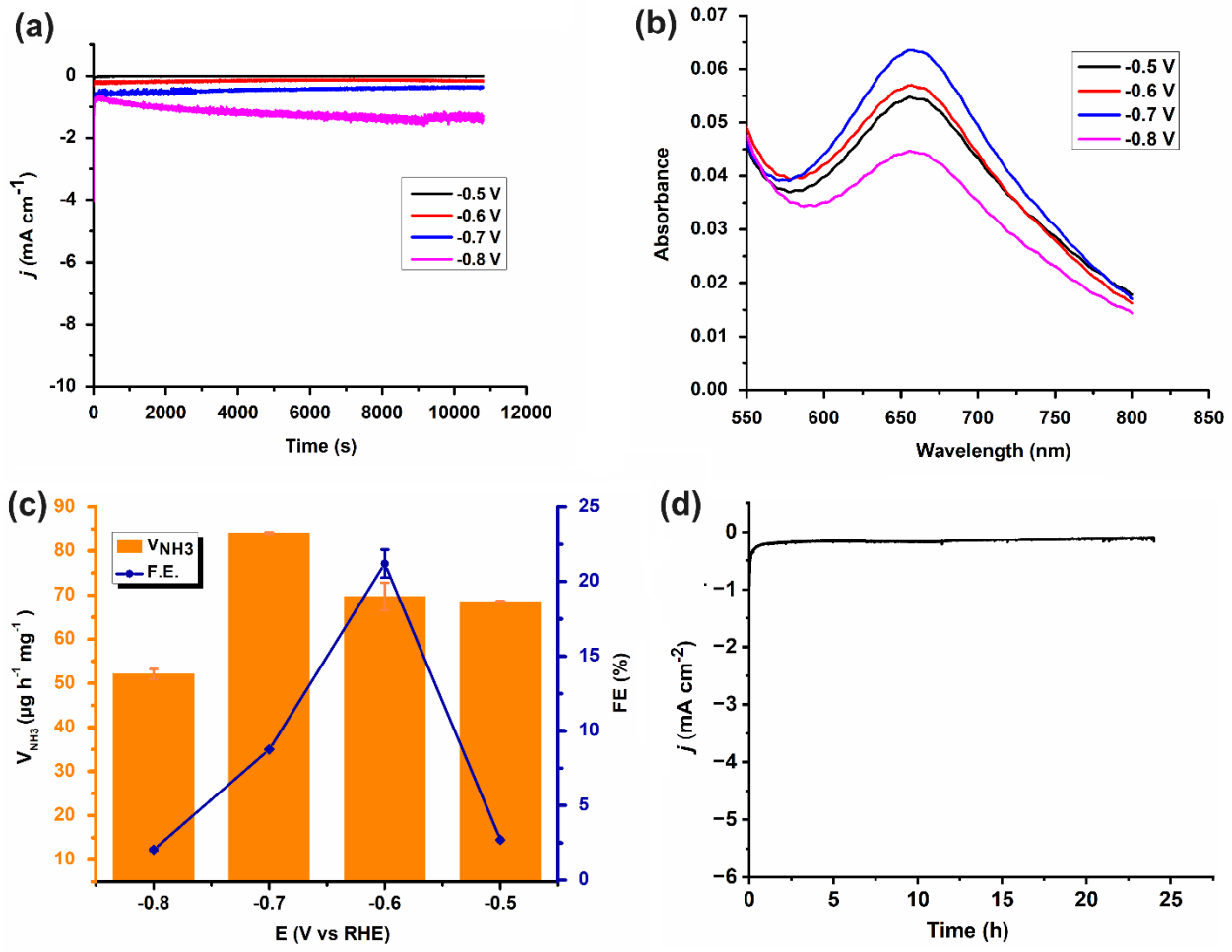

Figure 7. (a) Chronoamperometry results associated with C- ZrO_2-ZrN, collected at various potentials. (b) UV−visible absorption curves of the electrolytes using the indophenol method are shown after 3 h of electrolysis, measured against different potentials. (c) V_{NH3} and FE data for C-ZrO_2-ZrN are provided at each given potential. (d) Chronoamperometry data collected on C-ZrO_2-ZrN were measured at −0.7 V for 24 h.

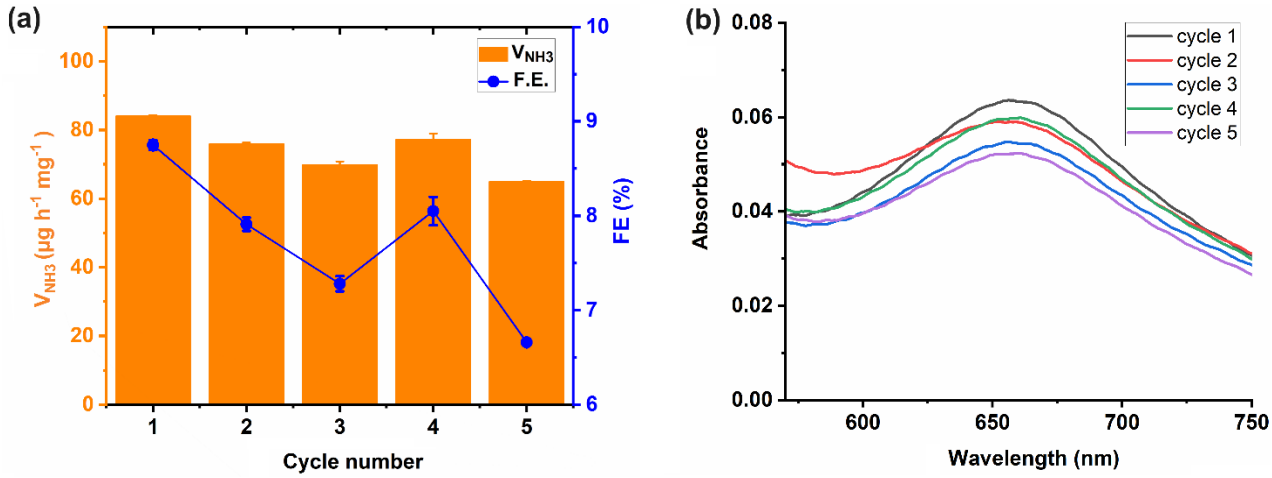

Figure 8. (a) Recycling test of C- ZrO_2-ZrN at −0.7 V and (b) corresponding UV−visible absorption curves for cycles 1 to 5.

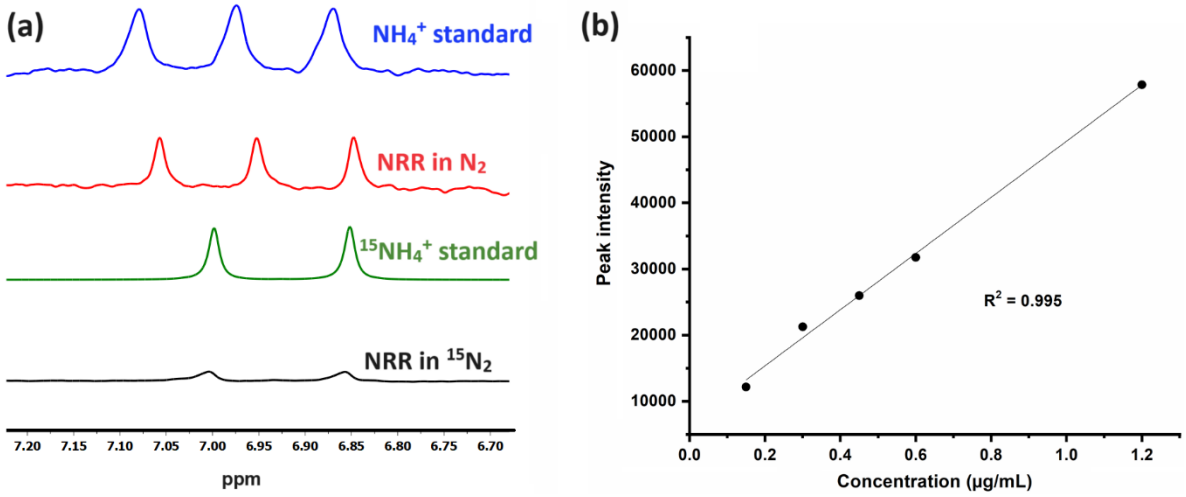

Figure 9. (a) ^{1}H NMR spectra (500 MHz) of NH_4^+, including NH_4^+ standard samples with concentrations of 1.2 μg mL^{-1} (blue curves), NRR samples after electrolysis at −0.7 V vs RHE using N_2 as the feeding gas (red curve), $^{15}NH_4^+$ standard samples with a concentration of 1.2 μg mL^{-1} (green curve), and NRR samples after electrolysis at −0.7 V vs RHE using $^{15}N_2$ as the feeding gas (black curve). **(b)** The calibration curve of the ^{1}H NMR signal at 6.97 ppm is given using standard solutions of varying concentrations of NH_4^+.

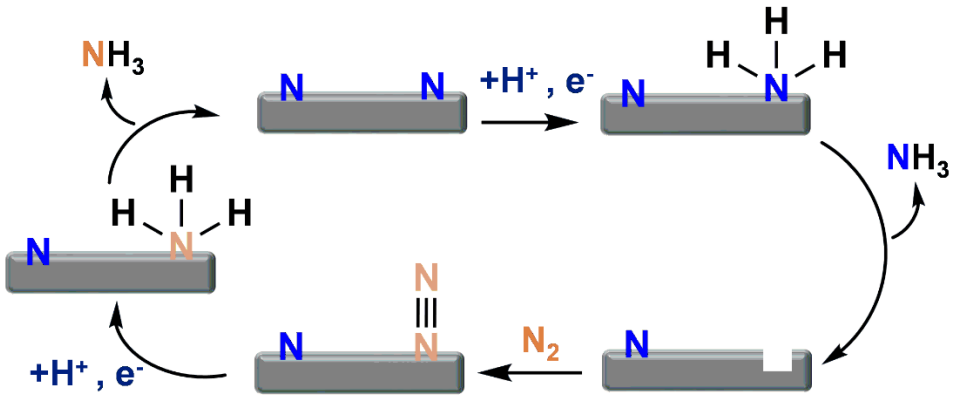

Figure 10. Proposed mechanism of possible electrochemical pathways for NRR on ZrO_2-ZrN electrocatalyst surface.

Table 1. Data used for the calculation of V_{NH3} and FE values for ZrO_2-ZrN@KB are provided to at most 3 significant digits. Error bars have also been added in, based on 3-5 replicate experimental runs performed at each potential.

E (V vs RHE)	Absorbance at ≈ 655 nm	$[NH_3]$ (μg/mL)	V_{NH3} (μg h^{-1} mg^{-1})	Q (mA•s)	FE (%)
-0.3	0.02	0.10	12.9 ± 0.9	4494	1.46 ± 0.09
-0.4	0.02	0.13	17.3 ± 0.4	5750	1.54 ± 0.04
-0.5	0.03	0.16	21.2 ± 0.8	13500	0.80 ± 0.03
-0.6	0.05	0.46	61.2 ± 0.5	69800	0.45 ± 0.002
-0.7	0.03	0.26	34.3 ± 3.9	91200	0.19 ± 0.02
-0.8	0.03	0.16	24.3 ± 2.0	213000	0.05 ± 0.01

The volume of electrolyte used in all experiments was 40 mL, and the electrolysis time was 3 h.

Table 2. Data used for the calculation of V_{NH3} and FE values for ZrO_2-ZrN are provided to at most 3 significant digits. Error bars have also been added in, based on 3-5 replicate experimental runs performed at each potential.

E (V vs RHE)	Absorbance at ≈ 655 nm	$[NH_3]$ (μg/mL)	V_{NH3} (μg h^{-1} mg^{-1})	Q (mA•s)	FE (%)
-0.5	0.05	0.45	60.5 ± 0.07	1599	19.3 ± 0.005
-0.6	0.06	0.55	69.7 ± 3.12	1680	21.2 ± 0.94
-0.7	0.06	0.63	84.1 ± 0.17	4900	8.75 ± 0.02
-0.8	0.04	0.38	52.1 ± 1.12	13000	2.05 ± 0.04

The volume of electrolyte used in all experiments was 40 mL, and the electrolysis time was 3 h.